CRYSTAL PLASTICITY INSPIRED MODELLING OF FIBRE REINFORCED COMPOSITES

A Thesis Submitted to
the Graduate School of Engineering and Sciences of
İzmir Institute of Technology
in Partial Fulfillment of the Requirements for the Degree of

MASTER OF SCIENCE

in Civil Engineering

by
Emir Aybars DİZMAN

July 2022
İZMİR

ACKNOWLEDGMENTS

First and foremost, my deep and sincere gratitude is given to my advisor, Assoc. Prof. Dr. İzzet Özdemir for his encouragement, support, and patience throughout this study. He is truly the mentor to me who is sharing his wealth of knowledge, ideas, and experiences both on research and on life with me.

I would like to thank my thesis examining committee members, Assoc. Prof. Dr. Engin Aktaş and Assoc. Prof. Dr. Caner Şimşir for their precious comments on my study.

Finally, my special thanks to my parents, Dilek and Servet Dizman and my siblings for their caring and unconditional support in my whole life. I also would like to thank Aybüke who is always with me during all the happy and hard moments.

ABSTRACT

CRYSTAL PLASTICITY INSPIRED MODELLING OF FIBRE REINFORCED COMPOSITES

There is an increasing demand in carbon fibre reinforced (CFR) composites primarily due to their high strength-to-weight ratio. Although their single-ply behaviour is rather brittle (as compared to metals), by reducing the ply thickness and stacking differently oriented plies, brittleness is suppressed, and a ductile behaviour similar to metals is achieved.

In this thesis, a recently proposed material model inspired by crystal plasticity is reconsidered and implemented in an implicit finite element solution framework. To this end, a user-defined element is developed in a geometrically non-linear continuum setting and implemented in commercial finite element software Abaqus through UEL (User-defined ELement) subroutine. The model is validated by analytical solutions derived for simple shear cases and two experiments for different loading cases from the literature. The model is capable of predicting stress-strain response well in cases where matrix plasticity is dominant. Moreover, a parametric study on the cross-ply shear specimen is conducted to investigate the influence of different material parameters. In the last part, the model is extended by a continuum scale damage in the matrix and degradation in elastic material properties. The predictive capabilities of the damage extended model are assessed by re-analyzing the cross-ply shear test.

ÖZET

FİBER TAKVİYELİ KOMPOZİTLERİN KRİSTAL PLASTİSİTEDEN ESİNLENEREK MODELLENMESİ

Karbon Fiber Takviyeli (KFT) kompozitlere, özellikle yüksek mukavemet-ağırlık oranları nedeniyle artan bir talep vardır. Tek katmanlı davranışları (metallere kıyasla) oldukça gevrek olmasına rağmen, katman kalınlığı azaltılarak ve farklı fiber yönüne sahip katmanları birleştirerek bu gevreklik azaltılabilir ve bu sayede metallere benzer sünek bir davranış elde edilebilir.

Bu tezde, kristal plastisiteden esinlenerek yakın zamanda önerilen bir malzeme modeli yeniden ele alınmakta ve kapalı adım bir sonlu eleman çözümü çerçevesinde uygulanmaktadır. Bu amaçla, geometrik olarak doğrusal olmayan bir sürekli ortamda kullanıcı tanımlı bir eleman geliştirilmiş ve kullanıcı eleman (UEL) altprogramı aracılığıyla sonlu eleman yazılımı Abaqus'e entegre edilmiştir. Model, basit kesme durumları için türetilen analitik çözümler ve literatürden seçilen farklı yükleme durumları için iki deney ile doğrulanmıştır. Modelin matris plastisitesinin baskın olduğu durumlarda gerilim-gerinim tepkisini iyi tahmin etme yeteneğine sahip olduğu görülmüştür. Ayrıca, farklı malzeme parametrelerinin etkisini araştırmak için çapraz katlı kesme numunesi üzerinde parametrik bir çalışma yapılmıştır. Son bölümde, model, matriste süreklilik ölçeğinde hasar ve elastik malzeme özelliklerinde bozulmayı yansıtacak şekilde genişletilmiştir. Genişletilmiş hasar modelinin tahmin yetenekleri, çapraz katlı kesme testinin yeniden analiz edilmesiyle değerlendirilmiştir.

TABLE OF CONTENTS

LIST OF FIGURES

Figure **Page**

Figure **Page**

Figure **Page**

LIST OF TABLES

Table **Page**

CHAPTER 1

INTRODUCTION

Fibre Reinforced Composites (FRC) are lightweight and stiff materials used in various applications ranging from engineering structures to wind turbine blades. They are manufactured by the combination of at least two components with different properties in various proportions. This combination makes it possible to improve the properties of the constituent for the intended use. The high strength-to-weight ratio of the fibre reinforced composites has increased the demand for FRC's in the aforementioned disciplines. Due to this demand, mechanical response of these materials should be understood correctly. However, they are heterogeneous, so their characterization requires a large number of experiments. Since composites are expensive materials, successful modelling of composites would reduce the economic burden of experimental studies involving composites.

As far as modelling of composites is concerned, initially the interest was mostly on predicting the composite properties from the properties of the constituents (Nemat-Nasser et al., 2013). Afterwards, the emphasis shifted towards predicting the failure of composites. Typically, composites are observed to fail at low plastic strains and exhibit brittle-like behaviour. The modelling of failure mechanisms of composite materials attained priority and for this purpose an international event called World Wide Failure Exercise (WWFE) was organized (Hinton et al., 2002; Kaddour & Hinton, 2013). In this exercise, the theories on the modelling of composites were evaluated in all aspects by comparing with the experimental results.

Although, fibre reinforced composites are preferable for many properties, their brittle behaviour limits their use. In this context, there are studies in the literature on the effects of laminate thickness and fibre angle on the behaviour of composites. For example, the study of Ogihara and Nakatani (2012) reveals that the 48-ply composite exhibits more ductile behaviour than the 16-ply composite under monotonic tensile loading, although both specimens have the same thickness, please see Figure 1.1. Furthermore, Fuller and Wisnom (2018) shows that non-linearity increases with higher θ when monotonic tensile tests on $[\pm\theta]$ composite laminates are conducted.

In experimental studies conducted in recent years, elasto-plastic behaviour similar to that of metals has been observed in very thin plies, please see Figure 1.1. The modelling

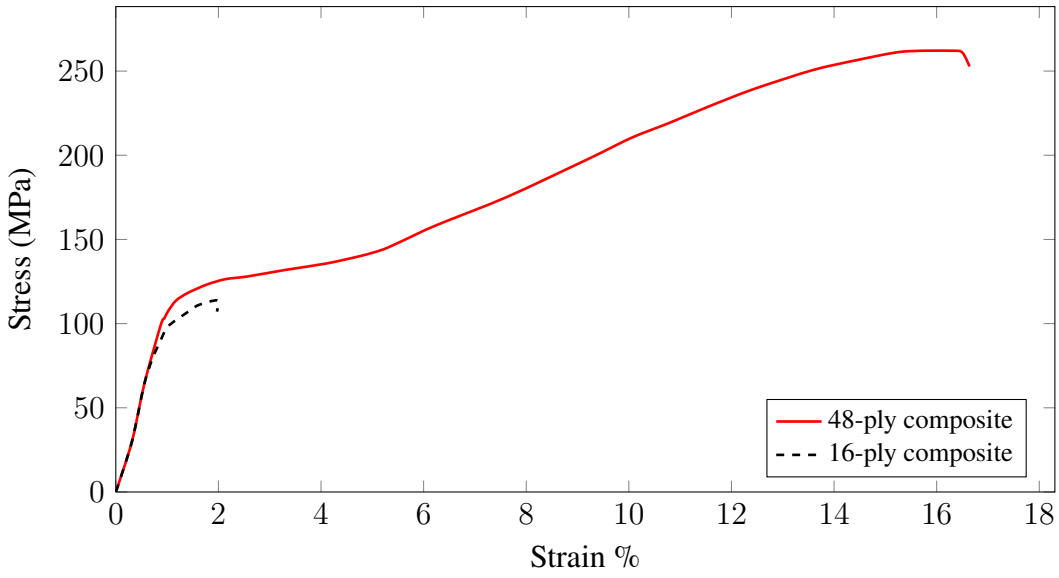

Figure 1.1. Comparison of stress-strain responses for different ply thickness (Source: Ogihara and Nakatani, 2012)

of this behaviour is an important issue and has been studied in recent years. Among the proposed models, especially the model inspired by crystal plasticity reproduces the experimental data quite well. Experiments on this subject show that plastic deformation of fibre in FRC has similarity to the notion of crystal plasticity. This similarity reveals that crystal plasticity can be a sensible approach to understand the plastic deformation of fibre reinforced composites. This modelling framework (Meza et al., 2019; Tan & Falzon, 2021; Tan & Liu, 2020) is proposed recently and its predictive capabilities and limitations are not fully explored yet.

1.1. Motivation of the Thesis

Departing from this point, the thesis focuses on crystal plasticity inspired modelling of composites. To this end, implicit version of the crystal plasticity based model proposed by Meza et al. (2019) is implemented in Abaqus through user defined element subroutine (UEL). The implementation is verified by using analytical solution of homogeneous tests and the predictions are compared with experimental results as well. Referring to Figure 1.2, it is clearly visible that the predictions deviate from the experimental results at relatively high strain levels. This is essentially attributed to damage mechanisms taking place within the matrix, fibre and matrix-fibre interface. To address this, in the last part of the thesis, the model is extended to include matrix damage using the concepts of continuum damage mechanics.

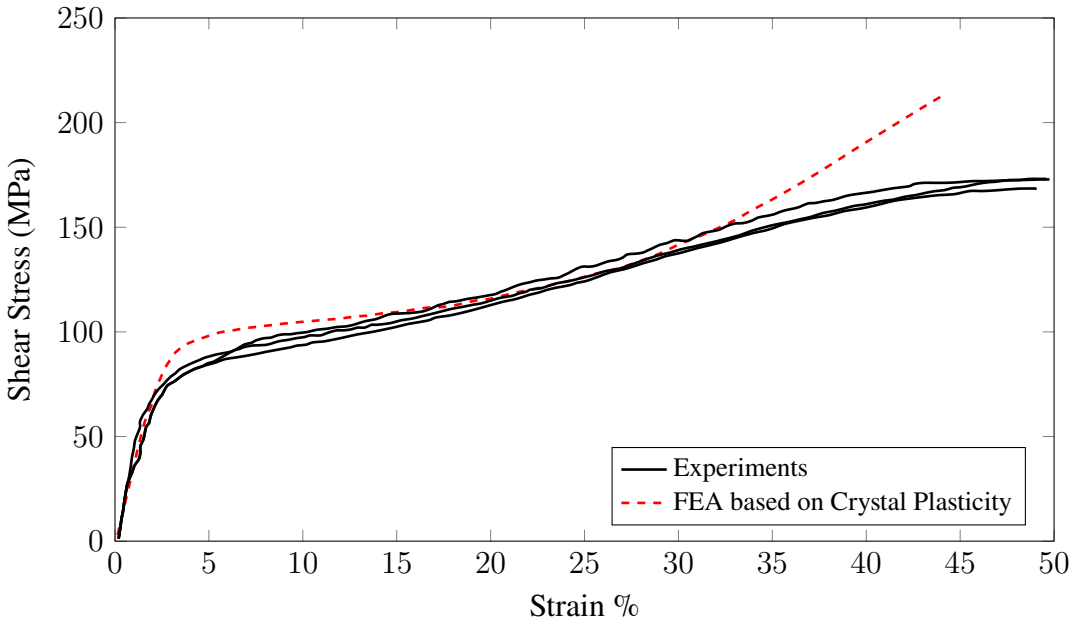

Figure 1.2. Measured and predicted shear stress-strain responses of $[\pm 90]_{4s}$ (Source: Tan and Falzon (2021))

In the next chapter, crystal plasticity inspired model and its adoption to composites is explained. The following chapter deals with the implementation of the model and elaborates on its algorithmic structure. Simple shear tests and comparison with experimental results are presented in this chapter. In the next chapter, it is explained how the concepts of damage mechanics are connected to the model and implemented. The effect of damage on predictions is investigated by repeating the analysis with the damage-extended model. Finally the thesis is closed by Conclusion & Outlook chapter.

CHAPTER 2

CRYSTAL PLASTICITY INSPIRED MODELLING OF COMPOSITES

2.1. Crystal Plasticity Theory

In this chapter, the primary goal is to give information about crystal plasticity theory and its adoption to fibre reinforced composites. In the vast majority of metals, plastic deformation results from dislocation glide. Crystal plasticity is an approach that tries to explain permanent deformation by incorporating crystalline level slip mechanisms. It postulates that permanent deformation occurs by shear at the microscopic level. According to this approach, plastic deformation is described as the sliding of atoms, and the specific planes on which the sliding occurs are called slip planes. These slip planes are defined by the direction vector $\vec{s}^{\eta}$ and the normal vector $\vec{n}^{\eta}$ of the slip plane, which are orthogonal to each other, see Figure 2.1 for illustrations of the slip systems.

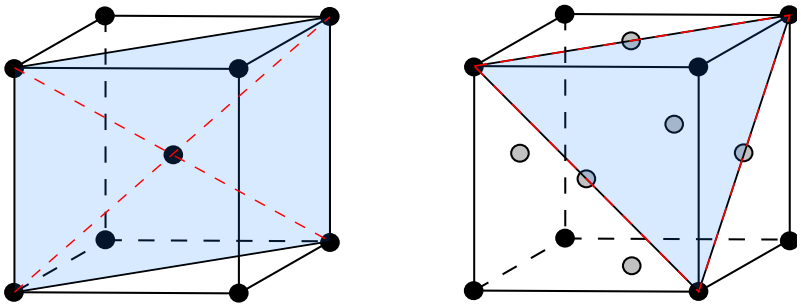

(a) (b)

Figure 2.1. An illustration for (a) Body Centred Cubic (BCC) slip system and (b) Face Centred Cubic (FCC) slip system.

Crystal plasticity is a continuum scale modelling approach based on these slip mechanisms and therefore has a strong physical basis. The kinematics of this description is going to be detailed in the next section.

2.1.1. Kinematics

The deformation gradient, $\mathbf{F}$ is the fundamental measure of deformation in continuum mechanics. It is the second-order tensor that maps material line elements in the reference configuration into line elements in the current configuration. The mapping is expressed mathematically as,

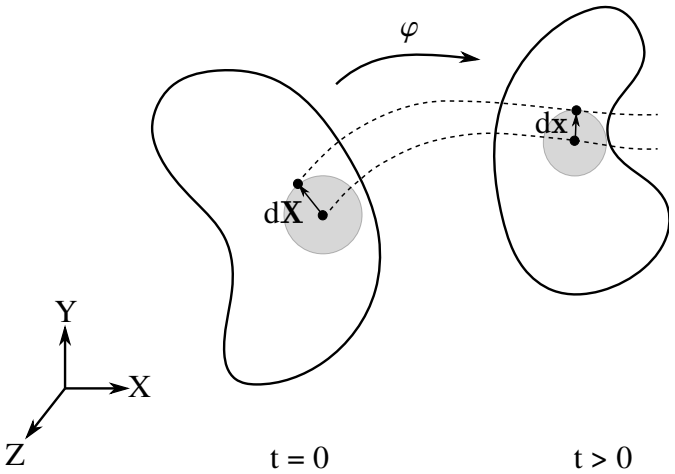

Figure 2.2. Line segment mapping of a deformable body.

$$\mathrm{d}\mathbf{x} = \mathbf{F}\,\mathrm{d}\mathbf{X} \tag{2.1}$$

In finite strain crystal plasticity, total deformation gradient tensor is split into an elastic and a plastic part,

$$\mathbf{F} = \mathbf{F}_\mathrm{e}\,\mathbf{F}_\mathrm{p} \qquad \det(\mathbf{F}_\mathrm{e}) > 0 \quad \& \quad \det(\mathbf{F}_\mathrm{p}) = 1 \tag{2.2}$$

which is called as multiplicative decomposition of deformation gradient. This decomposition implies that there is a fictitious intermediate state formed by plastic deformation gradient tensor, please see Figure 2.3. The plastic part consists of plastic slips on the slip planes, whereas the elastic part is composed of lattice distortion and rotation. In intermediate state, the lattice structure is the same as the undeformed configuration and the slip vectors do not alter. The rotation and stretching of slip vectors take place as a result of elastic part of deformation gradient. Current slip vectors are evaluated by $\vec{s}^{\,\eta} = \mathbf{F}_\mathrm{e}\,\vec{s}_0^{\,\eta}$ and $\vec{n}^{\,\eta} = \mathbf{F}_\mathrm{e}^{-\mathrm{T}}\,\vec{n}_0^{\,\eta}$, both are orthogonal.

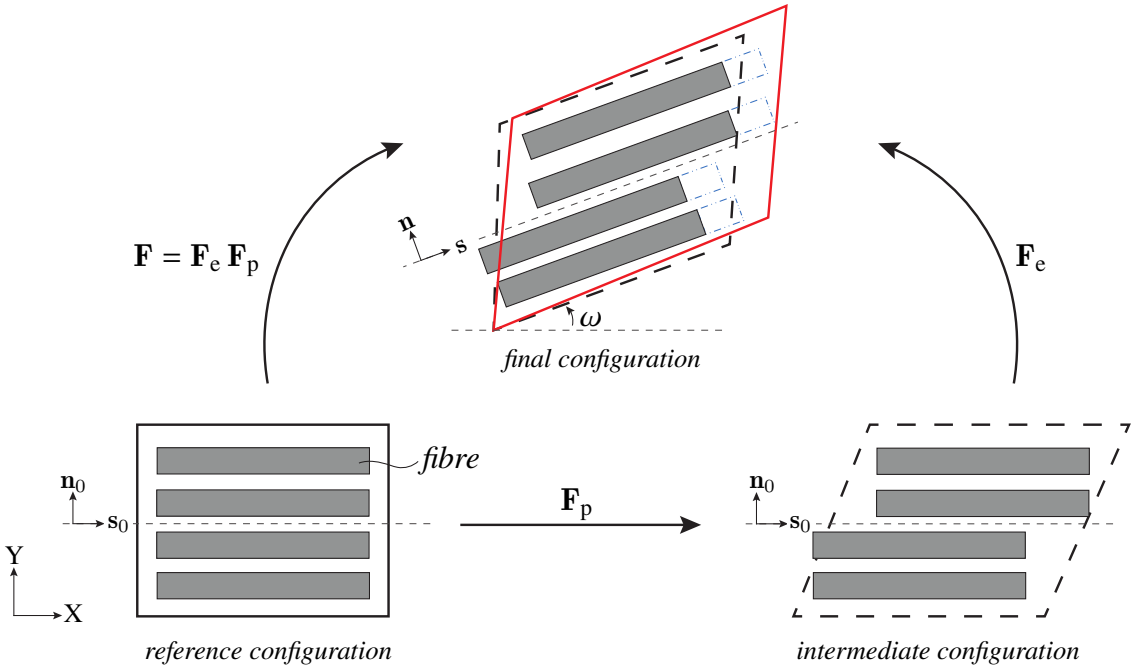

Figure 2.3. Please note that the slip vector in reference configuration and intermediate configuration are identical. Dashed black lines in the final configuration are obtained by mapping $\mathbf{R}_e$ and the solid red line represents the final configuration.

The fibre rotation due to deformation, denoted as ω in Figure 2.3, can be evaluated based on elastic rotation tensor. With polar decomposition, a deformation gradient can be multiplicatively decomposed into orthogonal rotation and symmetric stretch tensors. Polar decomposition of elastic deformation gradient can be expressed as,

$$\mathbf{F}_e = \mathbf{R}_e \, \mathbf{U}_e \tag{2.3}$$

where $\mathbf{R}_e$ and $\mathbf{U}_e$ are elastic rotation tensor and elastic stretch tensor, respectively. Right Cauchy-Green deformation tensor corresponding to $\mathbf{F}_e$ can be written as

$$\mathbf{C}_e = {\mathbf{F}_e}^{\mathrm{T}} \mathbf{F}_e = \mathbf{U}_e \underbrace{\mathbf{R}_e^{\mathrm{T}} \mathbf{R}_e}_{\mathbf{I}} \mathbf{U}_e = \mathbf{U}_e \, \mathbf{U}_e \tag{2.4}$$

which is used to obtain $\mathbf{U}_e$ through spectral decomposition as

$$\mathbf{U}_e = \sqrt{\lambda_1}\, \mathbf{n}_1 \otimes \mathbf{n}_1 + \sqrt{\lambda_2}\, \mathbf{n}_2 \otimes \mathbf{n}_2 + \sqrt{\lambda_3}\, \mathbf{n}_3 \otimes \mathbf{n}_3 \tag{2.5}$$

where λ_i, $\mathbf{n}_i$ are eigenvalues and eigenvectors of $\mathbf{C}_e$, respectively. After getting $\mathbf{U}_e$, $\mathbf{R}_e$

can be easily calculated by

$$\mathbf{R}_\mathrm{e} = \mathbf{F}_\mathrm{e}\,\mathbf{U}_\mathrm{e}^{-1} \tag{2.6}$$

In almost all experimental studies, fibre directions vary around an axis perpendicular to the plane of the ply, i.e. z-axis according to Figure 2.3. Therefore, elastic rotation tensor has the following form,

$$\mathbf{R}_\mathrm{e} = \begin{bmatrix} \cos\omega & -\sin\omega & 0 \\ \sin\omega & \cos\omega & 0 \\ 0 & 0 & 1 \end{bmatrix} \tag{2.7}$$

from which the rotation angle of fibres around z-axis can be calculated as,

$$\omega = \tan^{-1}\left(\frac{(\mathbf{R}_\mathrm{e})_{21}}{(\mathbf{R}_\mathrm{e})_{11}}\right) \tag{2.8}$$

When the material deforms, there must be differences in velocity between adjacent points which cause a gradient in the velocity field called as spatial velocity gradient tensor $\boldsymbol{\ell}$ and written as,

$$\frac{\partial}{\partial t}(\mathrm{d}\mathbf{x}) = \dot{\mathbf{F}}\,\mathrm{d}\mathbf{X} = \underbrace{\dot{\mathbf{F}}\,\mathbf{F}^{-1}}_{\boldsymbol{\ell}}\,\mathrm{d}\mathbf{x} \tag{2.9}$$

Inserting multiplicative decomposition into Equation 2.9 leads to the additive decomposition of $\boldsymbol{\ell}$ as,

$$\boldsymbol{\ell} = \boldsymbol{\ell}_\mathrm{e} + \dot{\mathbf{F}}_\mathrm{e}\,\boldsymbol{\ell}_\mathrm{p}\,\mathbf{F}_\mathrm{e}^{-1} \tag{2.10}$$

where,

$$\boldsymbol{\ell}_\mathrm{e} = \dot{\mathbf{F}}_\mathrm{e}\mathbf{F}_\mathrm{e}^{-1} \quad \& \quad \boldsymbol{\ell}_\mathrm{p} = \dot{\mathbf{F}}_\mathrm{p}\mathbf{F}_\mathrm{p}^{-1} \tag{2.11}$$

are the elastic and plastic velocity gradient tensors, respectively. In crystal plasticity, $\boldsymbol{\ell}_p$ is defined as,

$$\boldsymbol{\ell}_\mathrm{p} = \sum_{\eta=1}^{n_{slip}} \dot{\gamma}^\eta\,\vec{s}_0^{\,\eta} \otimes \vec{n}_0^{\,\eta} \tag{2.12}$$

which is the summation of slip rates on specific slip planes identified by η. Inserting this into Equation 2.11 results in the following evolution equation for $\mathbf{F}_\mathrm{p}$

$$\dot{\mathbf{F}}_\mathrm{p} = \sum_{\eta=1}^{n_{slip}} \dot{\gamma}^\eta \left(\vec{s}_0^{\,\eta} \otimes \vec{n}_0^{\,\eta}\right) \mathbf{F}_\mathrm{p} \tag{2.13}$$

which is updated mostly by using exponential map algorithm, see de Souza Neto et al. (2011). Once $\mathbf{F}_\mathrm{p}$ is updated and available, elastic deformation gradient is obtained by inserting $\mathbf{F}_\mathrm{p}$ into Equation 2.2. Following this, Green strain tensor is calculated as

$$\mathbf{E} = \frac{1}{2}(\mathbf{C}_\mathrm{e} - \mathbf{I}) \tag{2.14}$$

where $\mathbf{C}_\mathrm{e} = \mathbf{F}_\mathrm{e}^\mathrm{T}\mathbf{F}_\mathrm{e}$. Thereafter, the second Piola–Kirchhoff (P-K) stress tensor is calculated by $\mathbf{S} = \mathbb{C} : \mathbf{E}$ where $\mathbb{C}$ is the forth-order constitutive tensor.

As far as the adoption of this model to composites is concerned, there are a number of issues that have to be addressed. The first issue is the determination of slip systems (slip angles) for composites. There are essentially two factors which are used to specify these planes. The first one is the fibre arrangement which could be seen in an idealized form in Figure 2.4. In case of hexagonal closed packed fibre arrangement, slip angle for transverse system is identified as $\pm 30°$. However, if the fibre arrangement is different, other slip planes may exist and depends on the failure criteria considered. Tan and Liu (2020) carried out finite element analysis of transverse compression test with different slip angles. The results of these analyses, please see Figure 2.5, suggest that $\beta = 45°$ yields the closest initial yield stress to experimental result.

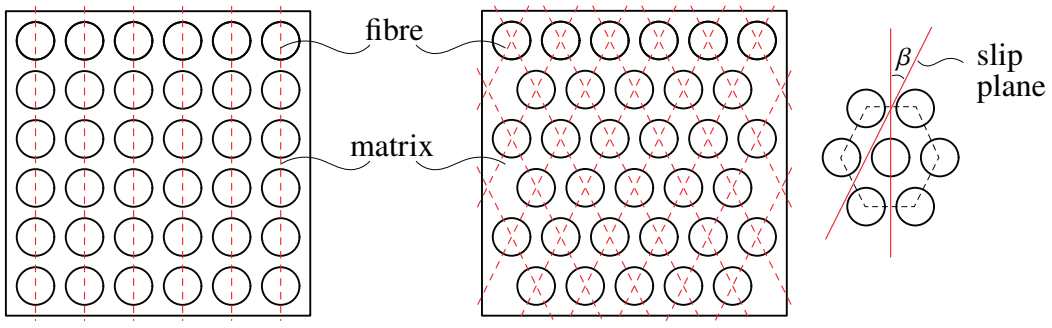

Figure 2.4. (a) Square and (b) hexagonal ($\beta = 30°$) arrangement of fibres.

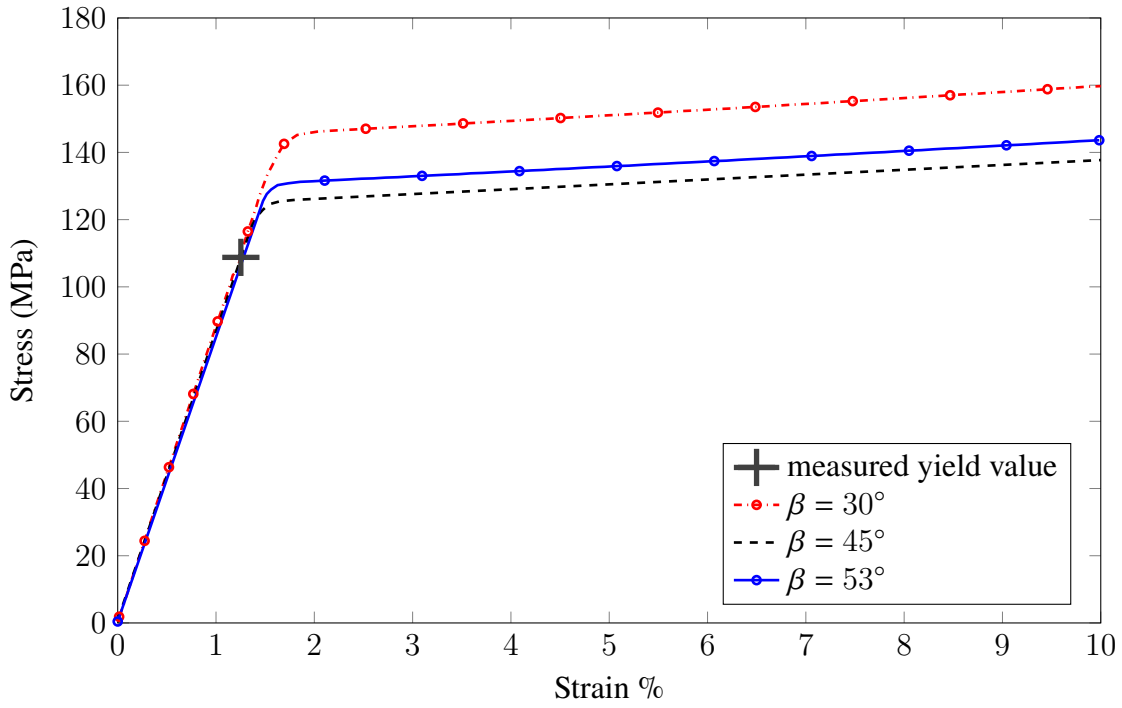

Figure 2.5. Stress – strain responses of unidirectional lamina for 3 different slip angles under transverse compression. (Source: Tan and Liu, 2020)

As mentioned before, the slip planes for a FRC are split into two classes as longitudinal and transverse slip systems. Systems whose slip direction is parallel to the fibre direction are classified as longitudinal, while systems that are perpendicular are defined as transverse. These slip systems are shown in Figure 2.6 and the slip vectors are given in Table 2.1. Slip systems are used in the definition of $\boldsymbol{\ell}_p$.

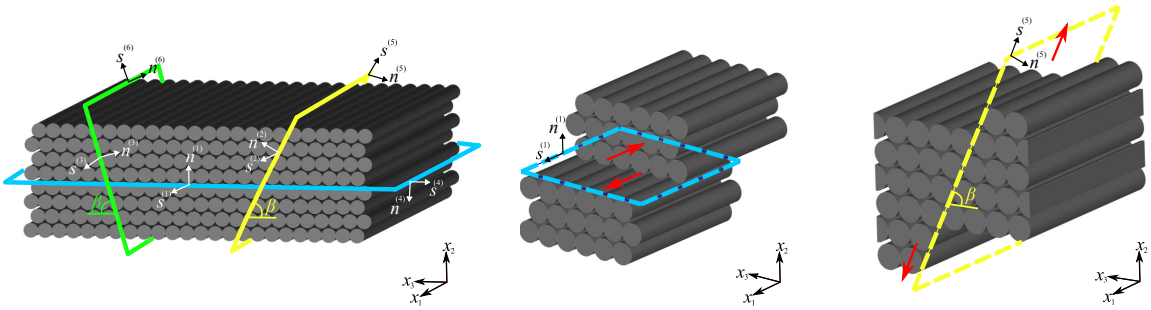

Figure 2.6. An illustration of slip systems reproduced from Tan and Liu (2020)

Table 2.1. Slip systems

System number (type)	$\vec{s}_0$	$\vec{n}_0$
1 (longitudinal)	$(1 \quad 0 \quad 0)$	$(0 \quad 1 \quad 0)$
2 (longitudinal)	$(1 \quad 0 \quad 0)$	$(0 \quad \cos\beta \quad \sin\beta)$
3 (longitudinal)	$(1 \quad 0 \quad 0)$	$(0 \quad \cos\beta \quad -\sin\beta)$
4 (transverse)	$(0 \quad 0 \quad -1)$	$(0 \quad -1 \quad 0)$
5 (transverse)	$(0 \quad \sin\beta \quad -\cos\beta)$	$(0 \quad -\cos\beta \quad -\sin\beta)$
6 (transverse)	$(0 \quad \sin\beta \quad \cos\beta)$	$(0 \quad \cos\beta \quad -\sin\beta)$

Since the micro-structure is transversely isotropic, the elastic response is governed by the following compliance relation,

$$\underbrace{\begin{bmatrix} \mathrm{E}_{11} \\ \mathrm{E}_{22} \\ \mathrm{E}_{33} \\ \mathrm{E}_{12} \\ \mathrm{E}_{13} \\ \mathrm{E}_{23} \end{bmatrix}}_{\mathbf{E}} = \underbrace{\begin{bmatrix} 1/E_f & -\nu_{21}/E_{m2} & -\nu_{31}/E_{m3} & 0 & 0 & 0 \\ -\nu_{12}/E_f & 1/E_{m2} & -\nu_{32}/E_{m3} & 0 & 0 & 0 \\ -\nu_{13}/E_f & -\nu_{23}/E_{m2} & 1/E_{m3} & 0 & 0 & 0 \\ 0 & 0 & 0 & 1/(2G_{12}) & 0 & 0 \\ 0 & 0 & 0 & 0 & 1/(2G_{13}) & 0 \\ 0 & 0 & 0 & 0 & 0 & 1/(2G_{23}) \end{bmatrix}}_{\mathbf{H}} \underbrace{\begin{bmatrix} \mathrm{S}_{11} \\ \mathrm{S}_{22} \\ \mathrm{S}_{33} \\ \mathrm{S}_{12} \\ \mathrm{S}_{13} \\ \mathrm{S}_{23} \end{bmatrix}}_{\mathbf{S}} \tag{2.15}$$

$$\mathbf{S} = \mathbb{D} : \mathbf{E} \tag{2.16}$$

where E_f, E_{m2} and E_{m3} are Modulus of Elasticity of the material in longitudinal and transverse directions, respectively. The corresponding Poisson's Ratio and Shear Moduli are represented by ν_{ij} and G_{ij} where $i, j = 1, 2, 3$. By inverting Equation 2.15, the second Piola–Kirchhoff stress tensor is expressed in terms of material stiffness tensor $\mathbb{D}$ and Green strain tensor $\mathbf{E}$. In addition to this, slip evolution equation on individual slip systems is defined as

$$\dot{\gamma}^\eta = \dot{\gamma}_0^\eta \left(\frac{|\tau^\eta|}{g^\eta} \right)^{1/\mathrm{m}} \mathrm{sign}(\tau^\eta) \tag{2.17}$$

where τ^α is the Schmid stress driving the slip on that particular system. g^α is the resistance against slip and m is rate sensitivity exponent, Asaro and Needleman (1985). It is clear that a rate dependent viscous formulation is used here due to its relative easier implementation.

Schmid stress for each slip system is calculated by,

$$\tau^{\eta} = \boldsymbol{\tau} : (\vec{s}^{\,\eta} \otimes \vec{n}^{\eta}) = \vec{s}^{\,\eta}\, \boldsymbol{\tau}\, \vec{n}^{\eta} \tag{2.18}$$

where $\boldsymbol{\tau}$ is Kirchhoff stress tensor and obtained from second Piola-Kirchhoff stress tensor through

$$\boldsymbol{\tau} = \mathbf{F}_{\mathrm{e}}\, \mathbf{S}\, \mathbf{F}_{\mathrm{e}}^{\mathrm{T}} \tag{2.19}$$

The resistance against slip is represented by g^{α} and as opposed to metals, depends on confinement. The confining pressure is illustrated in Figure 2.7. In other words, the confining pressure (p) leads to an increase in resistance (like a friction mechanism) and expressed as,

$$g^{\eta} = \begin{cases} \tau_y^{\eta} + \mu\, \mathrm{p} & \mathrm{p} \geq 0 \\ \tau_y^{\eta} & \mathrm{p} < 0 \end{cases} \tag{2.20}$$

The aforementioned pressure on the fibres is calculated by averaging the local normal stresses S_{22} and S_{33},

$$\mathrm{p} = -\frac{1}{2}\left(\mathrm{S}_{22} + \mathrm{S}_{33}\right) \tag{2.21}$$

which are perpendicular to fibre direction as shown in Figure 2.7.

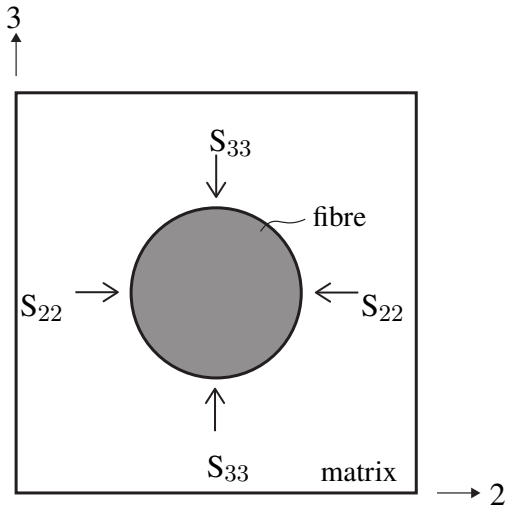

Figure 2.7. 2D drawing for the pressure from the matrix on the fibre.

Although various other plasticity models are available in the literature, the interest in using crystal plasticity in composites has recently increased. Classical plasticity models assume that the fibres' rotation follows the matrix's rotation under shear loading. However, the relative rotation difference between fibre and matrix reaches large values that cannot be neglected at high strains. Since crystal plasticity is inherently capable of capturing plastic spin, the crystal plasticity inspired models represent the micro-structure much better than classical plasticity models. In the next section, time discretization, i.e. stress update algorithm is presented.

2.1.2. Stress Update Algorithm

In an incremental-iterative solution framework, the intention of the stress-update algorithm is to find the stresses and the associated material tangent stiffness at t_{n+1}. Plastic deformation gradient $\left(\mathbf{F}_\mathrm{p}\right)_n$ and γ_n^η belonging to t_n are available. Furthermore the problem is displacement driven and an estimate for total deformation gradient $\mathbf{F}_{n+1}$ is available as well. By substituting $\Delta\gamma^\eta/\Delta t$ in place of $\dot{\gamma}^\eta$ in Equation 2.13, the equation can be rewritten as

$$\dot{\mathbf{F}}\,\mathbf{F}_\mathrm{p}^{-1} = \frac{1}{\Delta t}\sum_{\eta=1}^{6}\Delta\gamma^\eta\,\vec{s}_0^{\,\eta}\otimes\vec{n}_0^{\,\eta} \tag{2.22}$$

Using the exponential map, see for example de Souza Neto et al. (2011), plastic deformation gradient matrix in the current step can be written in terms of slip increments, reference slip systems and $\left(\mathbf{F}_\mathrm{p}\right)_n$ as

$$\left(\mathbf{F}_\mathrm{p}\right)_{n+1} = \mathbf{Q}\,\left(\mathbf{F}_\mathrm{p}\right)_n \quad \text{with} \quad \mathbf{Q} = \exp\left[\sum_{\eta=1}^{6}\Delta\gamma^\eta\,\vec{s}_0^{\,\eta}\otimes\vec{n}_0^{\,\eta}\right] \tag{2.23}$$

To calculate $\mathbf{Q}$ in Equation 2.23, the infinite series expansion given in de Souza Neto et al. (2011) is used by keeping the first six terms of the expansion. For further information please see Appendix B of de Souza Neto et al. (2011). Computation of the elastic deformation gradient tensor in the current step is done in a straightforward manner by using

$$\left(\mathbf{F}_\mathrm{e}\right)_{n+1} = \left(\mathbf{F}\right)_{n+1}\left(\mathbf{F}_\mathrm{p}\right)_{n+1}^{-1} \tag{2.24}$$

Since $\exp\left[\mathbf{A}\right]^{-1} = \exp\left[-\mathbf{A}\right]$ where $\mathbf{A}$ is a second-order tensor, $\left(\mathbf{F}_{\mathrm{p}}\right)_{n+1}^{-1}$ can be written as

$$\left(\mathbf{F}_{\mathrm{p}}\right)_{n+1}^{-1} = \left(\mathbf{F}_{\mathrm{p}}\right)_{n}^{-1} \exp\left[-\sum_{\eta=1}^{6} \Delta\gamma^{\eta} \vec{s}_0^{\,\eta} \otimes \vec{n}_0^{\,\eta}\right] \tag{2.25}$$

Elastic deformation gradient matrix is a key term in the process of crystal plasticity calculations. However, values of incremental slips $\Delta\gamma^{\eta}$ have to be determined. To this end, evolution equations are written in the following residual form which are enforced by Newton-Raphson method. Obtained residual equations are given as

$$r^{\eta} = \Delta\gamma^{\eta} - \Delta \mathrm{t}\, \dot{\gamma}_0^{\eta} \left(\frac{|\tau_{n+1}^{\eta}|}{g_{n+1}^{\eta}}\right)^{1/\mathrm{m}} \operatorname{sign}\left(\tau_{n+1}^{\eta}\right) = 0 \tag{2.26}$$

To solve the system of residual equations, the equations are linearized around iteration (k)

$$r^{\eta}|_k + \underbrace{\left.\frac{\partial r^{\eta}}{\partial \Delta\gamma^{\beta}}\right|_k}_{\mathbf{K}} \mathrm{d}\Delta\gamma^{\beta} = 0 \tag{2.27}$$

where $\mathbf{K}$ is the local tangent stiffness and the slip increments are updated by

$$\Delta\gamma_{k+1}^{\eta} = \Delta\gamma_{k}^{\eta} + \mathrm{d}\Delta\gamma^{\eta} \tag{2.28}$$

k and $\mathrm{d}\Delta\gamma^{\eta}$ refer to iteration number and corrective terms obtained from $\mathrm{d}\Delta\gamma^{\eta} = -\left(\mathbf{K}\right)^{-1} r^{\eta}$. The iterative local Newton-Raphson process is repeated until acceptable residual values are obtained. The general structure of the local Newton-Raphson algorithm is given in Algorithm 1. After completing the material level response, in the next section structural level behaviour is going to be discussed.

Algorithm 1 Local Newton-Raphson Algorithm

Initial estimate for slip increment on slip plane η, $\Delta\gamma_0^\eta = 0$

$\left(\mathbf{F}_\mathrm{e}\right)_{n+1} = \left(\mathbf{F}\right)_{n+1}\left(\mathbf{F}_\mathrm{p}\right)_{n+1}^{-1}$

$\mathbf{C}_{n+1} = \left(\mathbf{F}_\mathrm{e}\right)_{n+1}^\mathrm{T}\left(\mathbf{F}_\mathrm{e}\right)_{n+1}$

$\mathbf{E}_{n+1} = \frac{1}{2}\left(\mathbf{C} - \mathbf{I}\right)$

$\mathbf{S}_{n+1} = \mathbb{D} : \mathbf{E}_{n+1}$

$\boldsymbol{\tau}_{n+1} = \left(\mathbf{F}_\mathrm{e}\right)_{n+1}\mathbf{S}_{n+1}\left(\mathbf{F}_\mathrm{e}\right)_{n+1}^\mathrm{T}$

while norm $(\mathbf{r})$ > tolerance **do**

Calculate $\mathbf{K} = \frac{\mathrm{d}r^\eta}{\mathrm{d}\Delta\gamma^\beta}$

Update slip increments, $\Delta\gamma^\eta = \Delta\gamma^\eta + \mathrm{d}\Delta\gamma^\eta$

$\left(\mathbf{F}_\mathrm{e}\right)_{n+1} = \left(\mathbf{F}\right)_{n+1}\left(\mathbf{F}_\mathrm{p}\right)_{n+1}^{-1}$

$\mathbf{C}_{n+1} = \left(\mathbf{F}_\mathrm{e}\right)_{n+1}^\mathrm{T}\left(\mathbf{F}_\mathrm{e}\right)_{n+1}$

$\mathbf{E}_{n+1} = \frac{1}{2}\left(\mathbf{C} - \mathbf{I}\right)$

$\mathbf{S}_{n+1} = \mathbb{D} : \mathbf{E}_{n+1}$

$\boldsymbol{\tau}_{n+1} = \left(\mathbf{F}_\mathrm{e}\right)_{n+1}\mathbf{S}_{n+1}\left(\mathbf{F}_\mathrm{e}\right)_{n+1}^\mathrm{T}$

$\mathrm{r}^\eta = \Delta\gamma^\eta - \Delta\mathrm{t}\,\dot{\gamma}_0^\eta\left(\frac{|\tau_{n+1}^\eta|}{g_{n+1}^\eta}\right)^{1/\mathrm{m}}\mathrm{sign}\left(\tau_{n+1}^\eta\right)$

end while

2.2. Boundary Value Problem

At the structural level, the problem is in fact a boundary value problem which is governed by a partial differential equation and associated boundary conditions. The equation that is going to be solved is static equilibrium and written as,

$$\nabla\cdot\boldsymbol{\sigma} + \rho\,\mathbf{b} = \mathbf{0} \tag{2.29}$$

where $\nabla\cdot$ is the divergence operator with respect to current coordinates, ρ is the density and $\mathbf{b}$ is the body forces.

Since the analytical solutions are limited to simple geometries and boundary conditions, finite element method is used to solve the problem approximately. Following a weighted residual procedure, the weak form of the governing differential equation is obtained as,

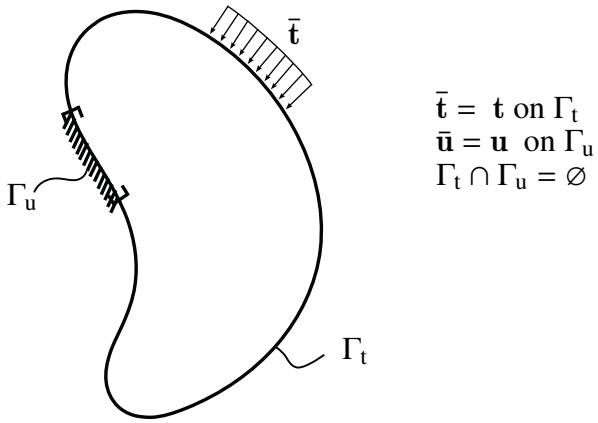

Figure 2.8. An illustration of a body with boundary conditions.

$$\underbrace{\int_v \boldsymbol{\sigma} : \nabla \delta \mathbf{u} \, \mathrm{d}v}_{\delta W_{int}} = \int_{\Gamma_t} \mathbf{t} \cdot \delta \mathbf{u} \, \mathrm{d}\Gamma_t + \int_v \rho \, \mathbf{b} \cdot \delta \mathbf{u} \, \mathrm{d}v \tag{2.30}$$

which in fact corresponds to the principle of virtual work. The internal virtual work at t_{n+1} can be written as,

$$\delta W_{int} = \int_V \boldsymbol{\tau}_{n+1} : \left(\nabla_0 \, \delta \mathbf{u} \left(\mathbf{F}^{-1} \right)_{n+1} \right) \mathrm{d}V \tag{2.31}$$

where the integral has to evaluated over the undeformed volume V. A brick type element with quadratic displacement interpolation (twenty-noded brick element) is used for spatial discretization. Using isoparametric finite element formulation, displacement gradient and gradient of virtual displacement can be written as,

$$\nabla_0 \mathbf{u} = \mathbf{B} \, \hat{\mathbf{u}}, \qquad \nabla_0 \delta \mathbf{u} = \mathbf{B} \; \delta \hat{\mathbf{u}} \tag{2.32}$$

where $\mathbf{B}$ is the matrix correlating nodal displacement degrees of freedoms ($\hat{\mathbf{u}}$ and $\delta\hat{\mathbf{u}}$) and gradient of displacement. Equation 2.30 can be written as,

$$\delta \hat{\mathbf{u}}^{\mathrm{T}} \left(\mathbf{f}_{int} - \mathbf{f}_{ext} \right) = 0 \tag{2.33}$$

which corresponds to $\mathbf{f}_{int} - \mathbf{f}_{ext} = \mathbf{0}$. The element level contribution to $\mathbf{f}_{int}$ is based on Equation 2.31 and reads as

$$\mathbf{f}_{int}^{\text{el}} = \int_{V_e} \mathbf{B}^{\mathrm{T}}\,\mathbf{P}\,\mathrm{dV} \tag{2.34}$$

where the 1st Piola-Kirchhoff tensor $\mathbf{P} = \boldsymbol{\tau}\,\mathbf{F}^{-\mathrm{T}}$. The virtual work equation is non-linear since both $\boldsymbol{\tau}$ and $\left(\nabla_0\,\delta\mathbf{u}\,\mathbf{F}^{-1}\right)$ depend on the displacement field; the unknowns of the problem. To solve a set of non-linear equations, δW_{int} should be linearized as

$$\mathrm{D}\big(\delta W_{int}\big)[\Delta\mathbf{u}] = \mathrm{D}\left(\boldsymbol{\tau}\right)[\Delta\mathbf{u}] : \nabla_0\delta\mathbf{u}\,\mathbf{F}^{-1} + \boldsymbol{\tau} : \mathrm{D}\big(\nabla_0\delta\mathbf{u}\,\mathbf{F}^{-1}\big)[\Delta\mathbf{u}] \tag{2.35}$$

in the direction of incremental displacements $\Delta\mathbf{u}$ and $\mathrm{D}(\,)\,[\Delta\mathbf{u}]$ represents the directional derivative. The first term on the right side of the equal sign produces material tangent stiffness, and the second one leads to geometric tangent stiffness. Expanding the second term leads to,

$$\mathrm{D}\big(\,\nabla_0\,\delta\mathbf{u}\mathbf{F}^{-1}\,\big)[\Delta\mathbf{u}] = \nabla_0\delta\mathbf{u}\;\mathrm{D}\big(\mathbf{F}^{-1}\big)[\Delta\mathbf{u}] \tag{2.36}$$

where $\mathrm{D}\big(\mathbf{F}^{-1}\big)[\Delta\mathbf{u}] = -\mathbf{F}^{-1}\,\mathrm{D}\big(\mathbf{F}\big)[\Delta\mathbf{u}]\,\mathbf{F}^{-1}$ and $\mathrm{D}\big(\mathbf{F}\big)[\Delta\mathbf{u}] = \mathbf{B}\,\big(\Delta\mathbf{u}\big)$. Expanding the first term leads to

$$\mathrm{D}\left(\boldsymbol{\tau}_{n+1}\right)[\Delta\mathbf{u}] \;=\; \underbrace{\frac{\partial\boldsymbol{\tau}_{n+1}}{\partial\mathbf{F}_{n+1}}}_{\left(\mathbb{D}_{\text{mat}}\right)_{n+1}}\;\mathrm{D}\big(\mathbf{F}_{n+1}\big)[\Delta\mathbf{u}] \tag{2.37}$$

Kirchhoff stress is a function of $\mathbf{F_e}$ and $\Delta\gamma^{\beta}$. Therefore, $\left(\mathbb{D}_{\text{mat}}\right)_{n+1}$ can be calculated by the chain rule as,

$$\frac{\partial\boldsymbol{\tau}_{n+1}}{\partial\mathbf{F}_{n+1}} = \frac{\partial\boldsymbol{\tau}_{n+1}}{\partial\left(\mathbf{F_e}\right)_{n+1}} : \frac{\partial\left(\mathbf{F_e}\right)_{n+1}}{\partial\mathbf{F}_{n+1}}\bigg|_{\Delta\gamma^{\beta}} + \frac{\partial\boldsymbol{\tau}_{n+1}}{\partial\left(\mathbf{F_e}\right)_{n+1}} : \frac{\partial\left(\mathbf{F_e}\right)_{n+1}}{\partial\Delta\gamma^{\beta}}\bigg|_{\mathbf{F}_{n+1}} : \frac{\partial\Delta\gamma^{\beta}}{\partial\mathbf{F}_{n+1}} \tag{2.38}$$

The derivations of the terms presented above are clearly demonstrated in Appendix-B. Rearranging the terms presented above, element tangent stiffness matrix can be written as

$$\mathbf{K}_{n+1}^{\text{el}} = \int_{V_e} \mathbf{B}^{\mathrm{T}}\left(\mathbf{C}_{\text{geo}}\right)_{n+1}\mathbf{B}\,\mathrm{dV} + \int_{V_e} \mathbf{B}^{\mathrm{T}}\left(\mathbf{C}_{\text{mat}}\right)_{n+1}\mathbf{B}\,\mathrm{dV} \tag{2.39}$$

where $\mathbf{C}_{\text{geo}}$ and $\mathbf{C}_{\text{mat}}$ are given in Appendix-B.

The general structure of global Newton-Raphson algorithm is presented in Algorithm 2.

Algorithm 2 Global Newton-Raphson Algorithm

Using $\left(\mathbf{F}\right)_{n+1}^{k}$, $\left(\mathbf{F}_{\mathrm{p}}\right)_{n}$, $\left(\gamma^{\eta}\right)_{n}$ calculate $\mathbf{P}_{n+1}$

(Please see Algorithm 1: Local Newton-Raphson Algorithm)

Calculate $\left(\mathbf{f}_{int}^{\mathrm{el}}\right)_{n+1} = \int \left(\mathbf{B}\right)_{n+1}^{\mathrm{T}} \mathbf{P}_{n+1} \mathrm{dV}$

Calculate $\left(\mathbf{f}_{ext}^{\mathrm{el}}\right)_{n+1}$

Assemble $\left(\mathbf{f}_{int}^{\mathrm{el}}\right)_{n+1}$ & $\left(\mathbf{f}_{ext}^{\mathrm{el}}\right)_{n+1}$ and obtain $\left(\mathbf{F}_{int}^{\mathrm{str}}\right)_{n+1}$ & $\left(\mathbf{F}_{ext}^{\mathrm{str}}\right)_{n+1}$

Calculate residual column $\mathbf{R}_{n+1} = \left(\mathbf{F}_{int}^{\mathrm{str}}\right)_{n+1} - \left(\mathbf{F}_{ext}^{\mathrm{str}}\right)_{n+1}$

while norm $\left(\mathbf{R}_{n+1}\right)$ > tolerance **do**

Calculate $\mathbf{K}_{n+1}^{\mathrm{el}} = \int \mathbf{B}^{\mathrm{T}} \left(\mathbf{C}_{\mathrm{geo}}\right)_{n+1} \mathbf{B}\, \mathrm{dV} + \int \mathbf{B}^{\mathrm{T}} \left(\mathbf{C}_{\mathrm{mat}}\right)_{n+1} \mathbf{B}\, \mathrm{dV}$

Assembly $\mathbf{K}_{n+1}^{\mathrm{str}}$

Solve for d$\mathbf{u}$

Update $\mathbf{u}|_{k+1} = \mathbf{u}|_{k} + \mathrm{d}\mathbf{u}$

Calculate $\mathbf{f}_{int}^{\mathrm{el}} = \int \mathbf{B}^{\mathrm{T}} \mathbf{P}_{n+1}\, \mathrm{dV}$

Assemble $\mathbf{f}_{int}^{\mathrm{el}}$ and obtain $\mathbf{F}_{int}^{\mathrm{str}}$

Calculate $\mathbf{R}_{n+1} = \mathbf{F}_{int}^{\mathrm{str}} - \mathbf{F}_{ext}^{\mathrm{str}}$

Calculate $||\mathbf{R}_{n+1}||$

end while

Update history variables, $\left(\mathbf{F}_{\mathrm{p}}\right)_{n} \leftarrow \left(\mathbf{F}_{\mathrm{p}}\right)_{n+1}$ & $\left(\gamma^{\eta}\right)_{n} \leftarrow \left(\gamma^{\eta}\right)_{n+1}$

Proceed with the next increment

CHAPTER 3

PERFORMANCE OF THE MODEL

3.1. Simple Shear Test

In this section, the implemented model is validated by analytical solution of simple shear test to verify the accuracy of stress-update algorithm. For this purpose, the finite element model, consisting of a single element with 1 mm x 1 mm dimensions and a thickness of 0.1 mm, is considered. The geometry of the model with expected deformed shapes are shown in Figure 3.1. In this context, two different fibre orientations are considered. In the first case, the displacement is imposed parallel to the fibre direction, while in the other, it is applied as perpendicular. It is aimed to have a homogeneous plane strain state with appropriate boundary conditions. Loading details for both models are presented in Section 3.1.1 and Section 3.1.2. The material parameters used in the model are given in Table 3.1.

Table 3.1. Model Parameters for IM7-8552 (Tan & Liu, 2020)

Material Parameter	Value
E_f	171420 MPa
E_m	8930 MPa
τ_y	62.3
μ	0.28
ν_{12}	0.32
ν_{13}	0.34
ν_{23}	0.34
G_{12}	5100 MPa

In Appendix-A, analytical solution for rate independent model is derived. Since the implemented material model is rate-dependent, rate-independent limit is obtained by setting m$\rightarrow$0. The rate sensitivity exponent is set to 0.0005 which makes the analysis result almost independent of the loading rate and provides almost an ideal elasto-plastic response. Considering that the analytical solution is 2D, the Poisson's ratio in the direction of y and z are taken as zero. Furthermore, out of plane displacement degrees of freedom

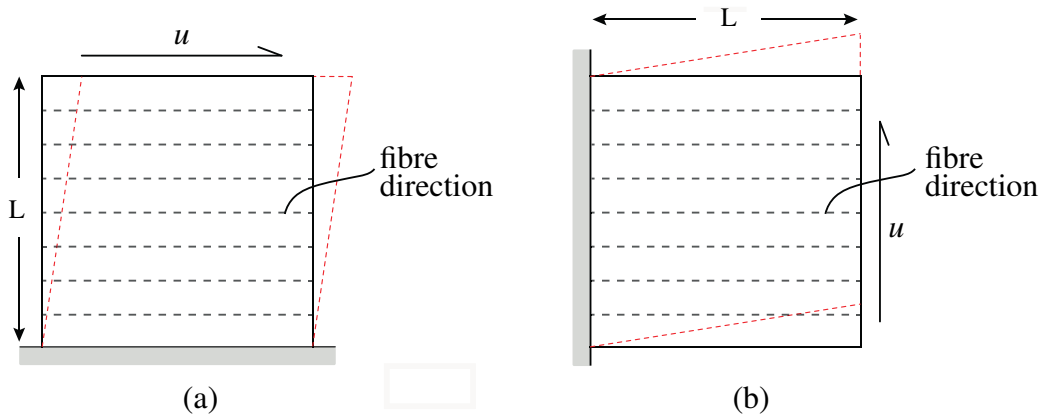

Figure 3.1. (a) Simple shear test for loading parallel to fibre direction (b) Simple shear test for loading perpendicular to fibre direction

of the model are set to zero so that plane strain conditions are imposed. Stress values are obtained by dividing the sum of the reaction forces by the surface area, and strain values are obtained by dividing the imposed displacement by height of the model L.

3.1.1. Loading Parallel to Fibre Direction

In the first case, the imposed displacement is parallel to the fibre direction. The finite element model and the corresponding displacement boundary conditions are shown in Figure 3.2a. Symmetry boundary conditions about the z-axis are defined for the back and front faces. Displacements at the bottom nodes are fixed in all directions. A displacement of 0.1 mm was applied to the upper nodes of the model, and a displacement of 0.05 mm was applied to the side mid-nodes. Therefore, linear displacement profile is imposed along the y direction. Second Piola-Kirchhoff stress components in each integration point are stored as an output, and stress distribution at the end of the analysis is presented in Figure 3.2b.

Figure 3.3 shows the stress-strain response obtained by finite element analysis of simple shear model. In order to reach the analytical solution valid for the rate-independent model, the analysis was repeated with 4 different values of m. Finite element model over-predicts the yield stress which is due to the fact that the analytical result is rate independent. By setting the rate sensitivity exponent as close as possible to zero, the response obtained from the finite element analysis gets very close to the analytical result.

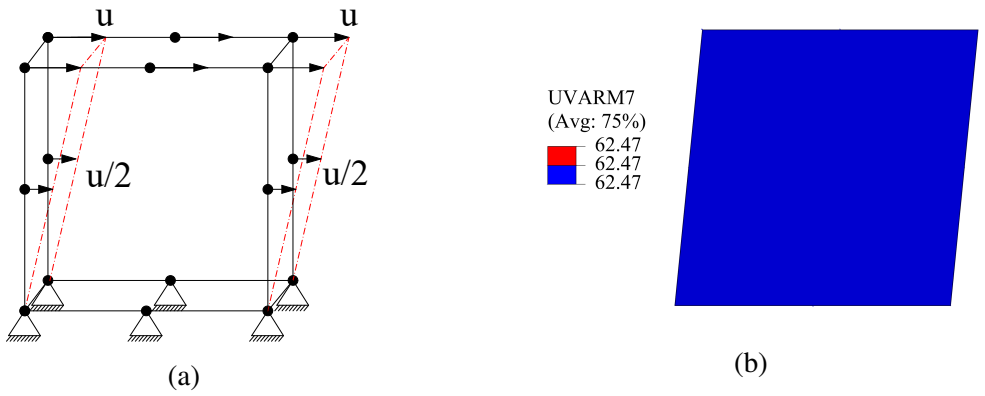

Figure 3.2. (a) Boundary conditions for the case of $\theta = 0°$ and (b) distribution of second Piola-Kirchhoff stress throughout the element.

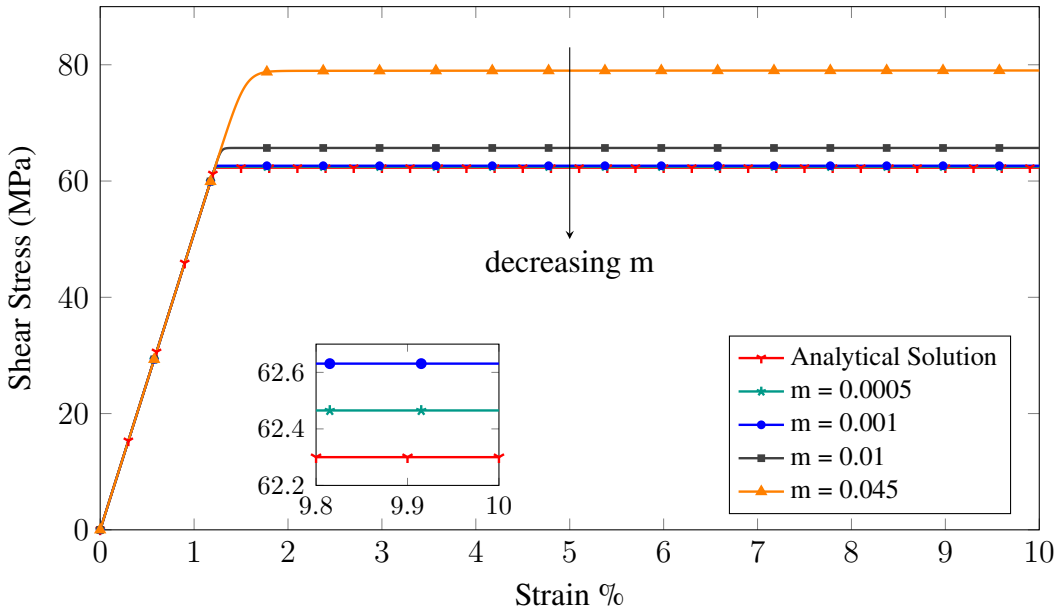

Figure 3.3. Comparison of finite element predictions and analytical solution for $\theta = 0°$ simple shear

3.1.2. Loading Perpendicular to Fibre Direction

In the second case, the prescribed displacement is perpendicular to the fibre direction. Symmetry boundary conditions about the z-axis are defined for the back and front faces. Displacements at the left edge nodes are prescribed in all directions. A displacement of 0.1 mm was applied to the right nodes of the model, and a displacement of 0.05 mm was applied to the top and bottom middle nodes. Thus, a gradually increasing displacement throughout the model is achieved. The defined boundary conditions for the

displacement are shown in Figure 3.4a. Second Piola-Kirchhoff stress contour through the model is exhibited in Figure 3.4b .

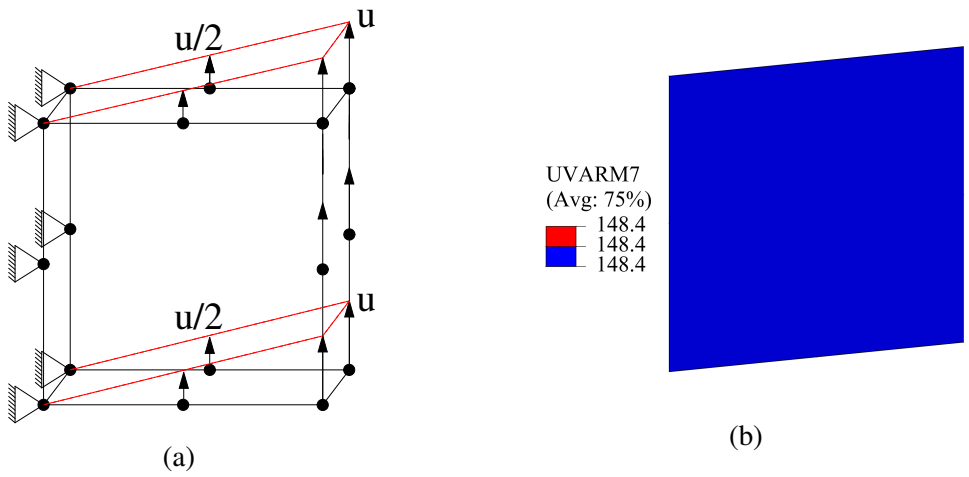

Figure 3.4. (a) Boundary conditions for the case of $\theta = 90°$ and (b) distribution of the second P-K stress throughout the element.

Figure 3.5 shows the stress-strain response obtained by finite element analysis. In order to approach the analytical solution, 4 different values of m are used. With m values approaching to zero, the model would become rate independent. It is obvious that the estimated result deviates somewhat from the analytical result more prominently at higher strain values. The reason of this deviation is that rate sensitivity exponent is very close to zero but still larger than 0. m=0.0005 is the smallest m value which the local Newton-Raphson algorithm could be completed successfully. In the analytical solution detailed in Appendix-A, hardening is observed in the presence of plastic strain when the loading direction is perpendicular to the fibre direction. Consistent with this expectation, hardening occurs beyond the initial yield stress in the finite element analysis results of the single-element model. The effect of longitudinal elastic modulus of composite on this hardening can be explained by the fact that deformation of the matrix is accompanied by the fibre rotation. This is also clearly visible in the Equation A.17.

3.2. Compression Test on Unidirectional Laminates

In the study of Koerber et al. (2010), the behaviour of uni-directional laminates with different fibre orientations under compression loading is investigated. The specimen has dimensions of 20 x 10 x 4 mm. It consists of 32 layers throughout the thickness, and

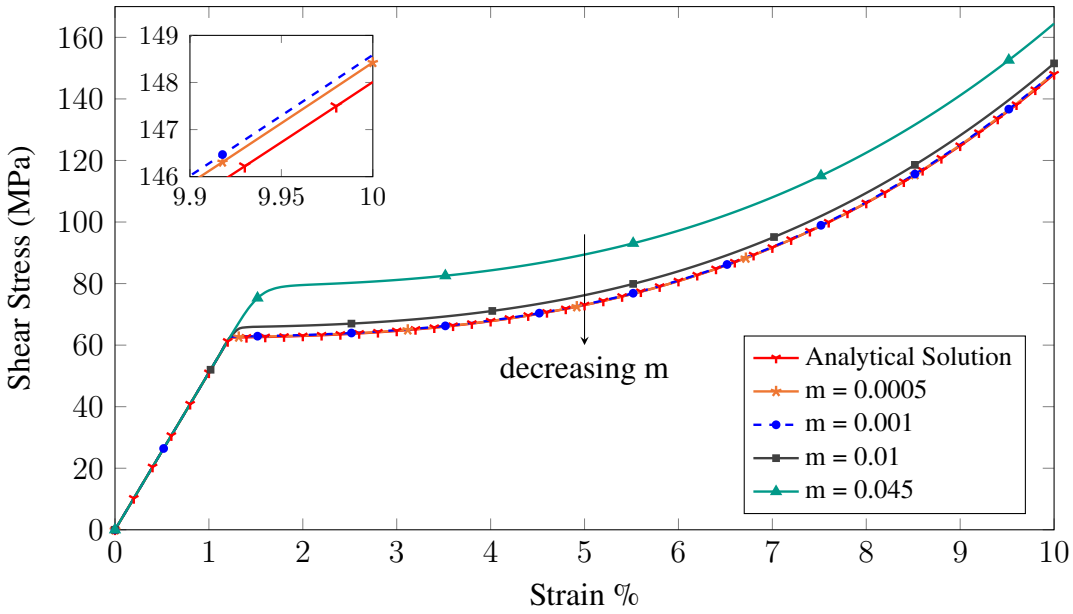

Figure 3.5. Comparison of finite element predictions and analytical solution for $\theta = 90°$ simple shear

the thickness of each layer is approximately 0.125 mm. Compression tests are carried for three different fibre angles of $0°$, $45°$ and $75°$. The orientation of the fibres is indicated as θ in Figure 3.6. End-loaded compression tests are conducted by INSTRON 4208 load frame. To reduce the friction between the loading surfaces and testing device, a thin layer of molybdenum-disulfide is used. The experimental loading rate, classified as quasi-static loading, is specified as 0.5 mm/min. The specimen consists of carbon fibres and epoxy resin that is designated as IM7. The material parameters used in all compression analysis are presented in Table 3.2.

Table 3.2. Model Parameters for IM7-8552 (Tan & Liu, 2020)

Material Parameter	Value
E_f	171420 MPa
E_m	8930 MPa
τ_y	62.3 MPa
μ	0.28
ν_{12}	0.32
ν_{13}	0.32
ν_{23}	0.34
G_{12}	5100 MPa
m	0.045

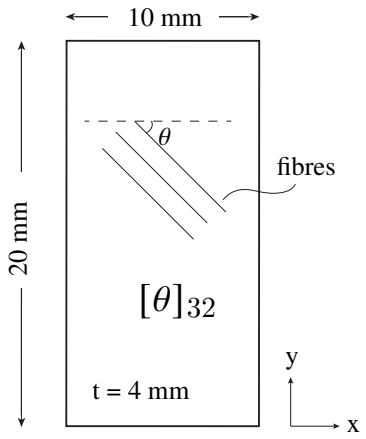

Figure 3.6. Geometry of $[\theta]_{32}$ Unidirectional Model

In the finite element analysis, the model is discretized by UEL which has the topology of twenty-noded quadratic brick element and has eight integration points. This element geometry and integration scheme corresponds to C3D20R of Abaqus library. A perfect bond is assumed between the ply laminates, so no internal contact or cohesive interaction is defined. In the finite element model, as in the experimental setup, a compression is applied to the specimen by two plates defined as rigid bodies. The friction between the specimen and rigid bodies are set to 0.001 in finite elements model to reflect low friction due to applied molybdenum-disulfide.

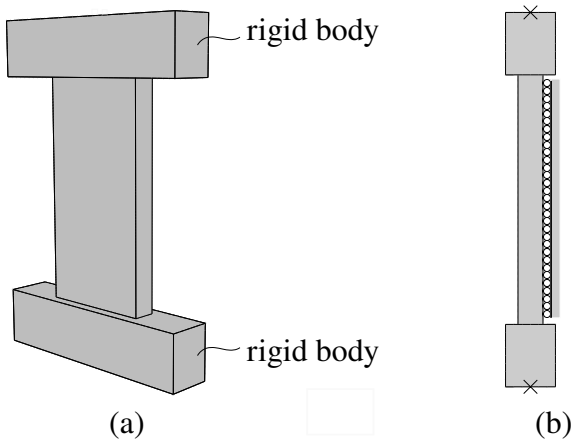

Figure 3.7. (a) An illustration for boundary conditions of $[\theta]_{32}$ unidirectional model (perspective view). (b) Symmetry boundary conditions in the z-direction on the back surface. Reference points are represented by crosses on the bottom and top rigid bodies (side view).

3.2.1. Compression Test on $\theta = 0^\circ$ Specimen

In the finite element model, degrees of freedoms at the bottom reference point is prescribed to zero whereas at the top reference point a displacement of 1.2 mm is applied along y-direction. Considering the loading rate in experiments, the step time for the prescribed displacement is set to 150 seconds. Three different element sizes are tested to check the mesh dependency and mesh convergence of the analysis, as shown in Figure 3.8. There is no remarkable difference between the responses of different element sizes. It indicates that the analysis is mesh independent. For that reason, medium-size structured mesh is used for further analysis.

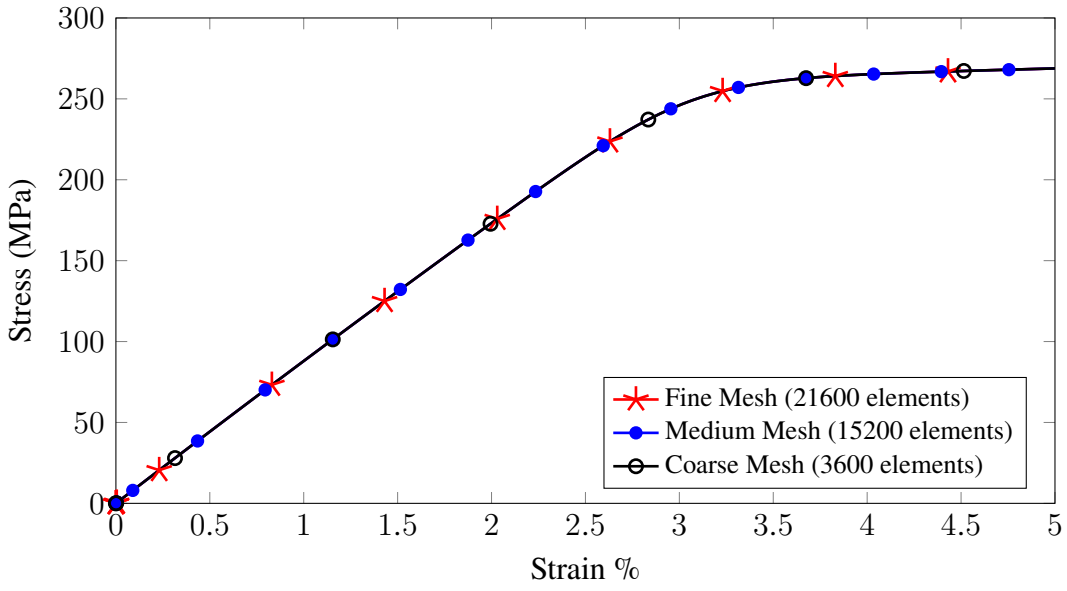

Figure 3.8. Mesh convergence of the model $\theta = 0°$ is investigated by 3 different element sizes.

Figure 3.9 illustrates the comparison of finite element analysis prediction with the experimental results for compression test of $[0°]_{32}$ model. Stress is calculated by dividing the applied force by the cross-sectional area. Initial tangent is identical with experimental results and the two curves are almost coincident until 1.5% strain level. While the FEA prediction overestimates the yield value, it produces a plateau-like behavior after 4% strain level.

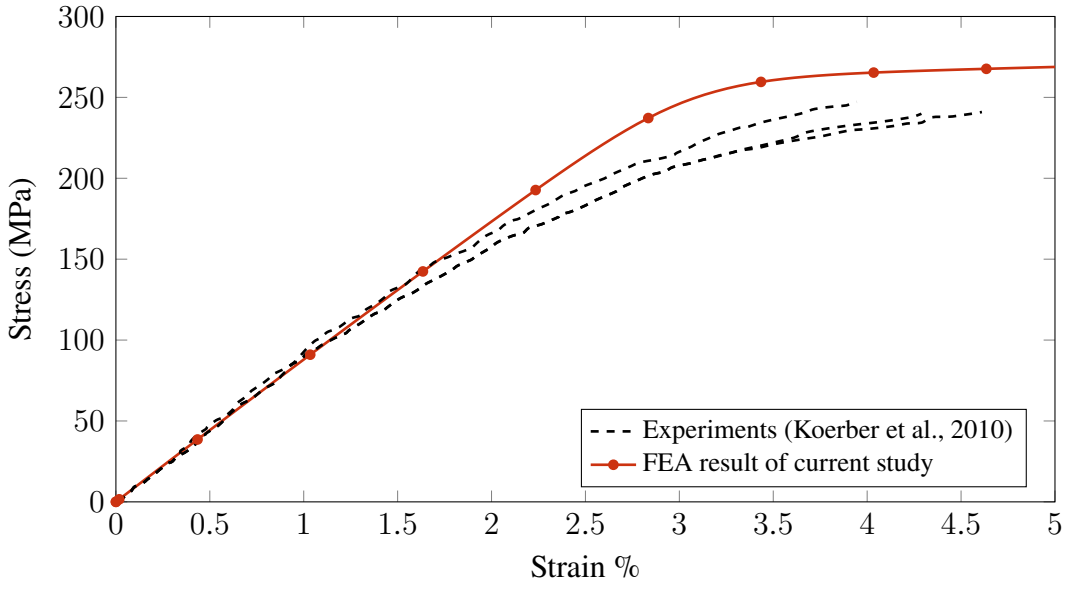

Figure 3.9. Comparison of simulation and the experimental results for $\theta = 0°$

Figure 3.10 shows slip systems in which the slip activities is observed the least and the most. While the slip occurring in the 6^{th} system is much larger compared to the other systems, the slip is non-existent in the system 1. The predicted axial strains are compared to digital image correlation (DIC) measurements in Figure 3.11. Although horizontal bands are obtained in finite element predictions, the strain distribution is almost uniform. However, the strain values are close to experimental results.

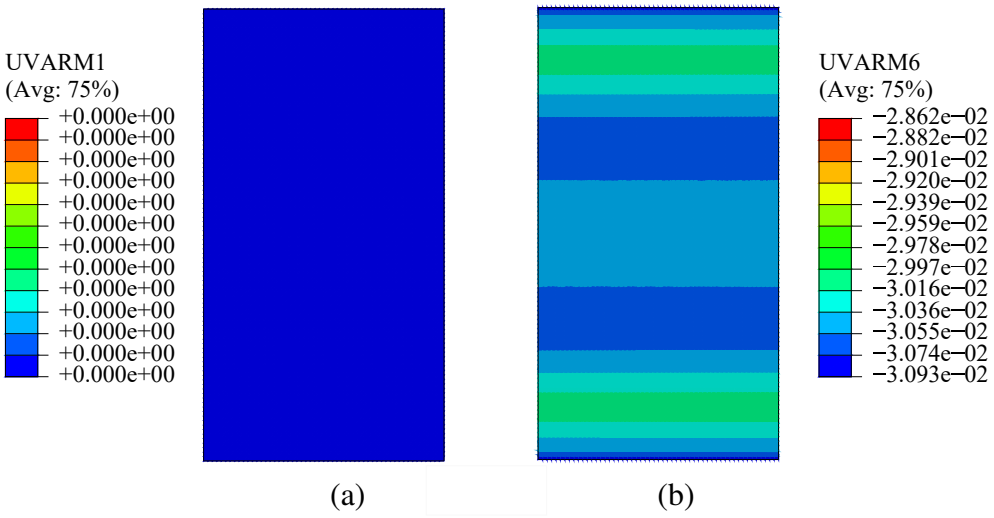

Figure 3.10. Minimum and maximum slip activities are observed in (a) slip system 1 and (b) slip system 6, respectively.

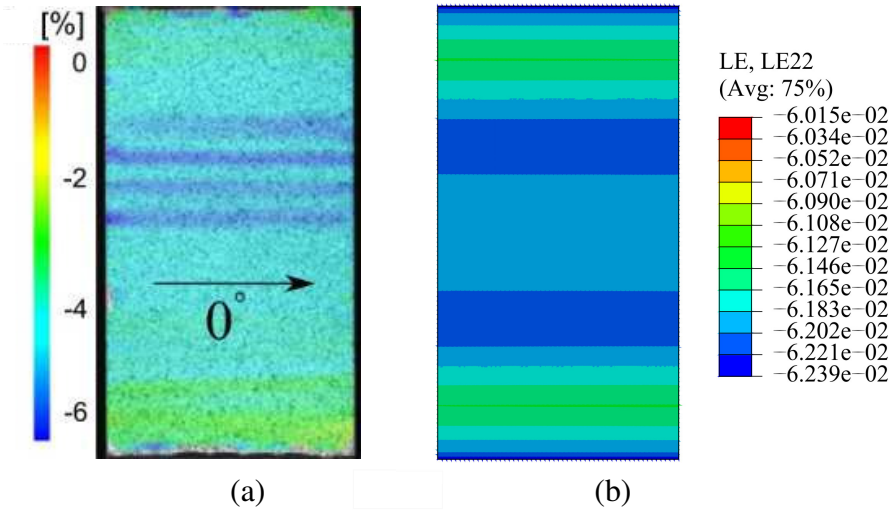

Figure 3.11. (a) ϵ_{22} obtained by Digital image correlation (DIC) measurement device (b) ϵ_{22} contour of finite element analysis

3.2.2. Compression Test on $\theta = 45^\circ$ Specimen

In the finite element model, the displacement degrees of freedoms at the bottom reference point are prescribed to zero, whereas a displacement of 2 mm in the y-direction is applied at the top reference point. Considering the loading rate in the experiments, the step time for the applied displacement is set to 250 seconds.

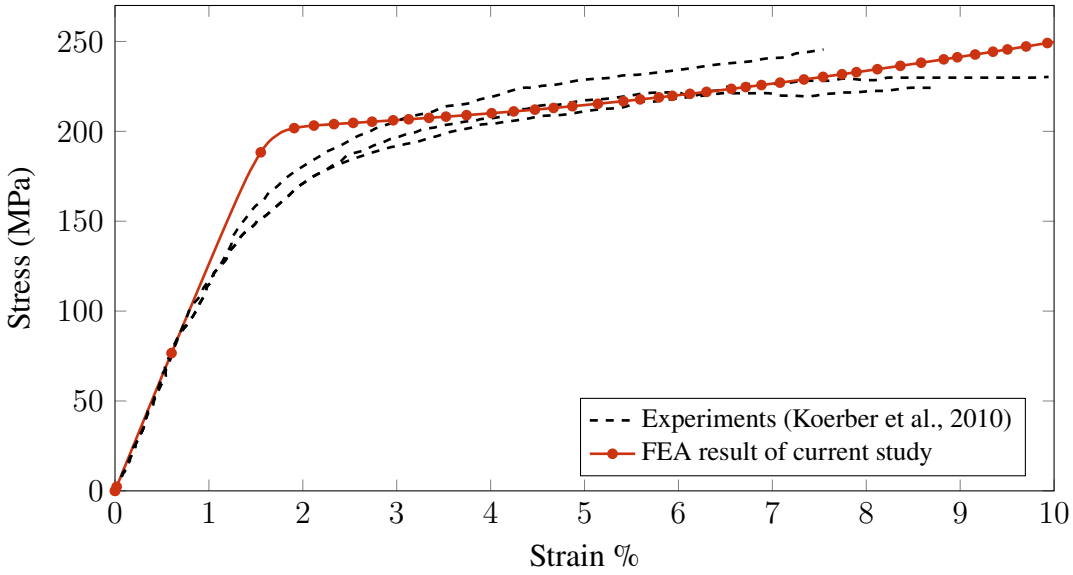

Figure 3.12. Comparison of simulation and the experimental results for $\theta = 45^\circ$

Figure 3.12 illustrates the comparison of finite element analysis result with the experimental results for compression test of $[45^\circ]_{32}$. Stress is calculated by dividing the applied force by the cross-sectional area of the specimen. There is a slightly upward tendency in the stress response beyond the 4% strain level similar to experimental observation. It is obvious that FEA predictions and experimental results are very close up to 1% strain levels. As in the previous case, FEA predictions overpredict the yield stress value. Figure 3.13 demonstrates that a diagonal band along fibre direction is observed similar to the one obtained by DIC measurement. The thickness of the band obtained in finite element analysis is approximately 4.8 mm whereas it is more or less equal to observed in the experimental results. Contrary to the DIC measurements, the strain occurring in the upper right and lower left corners exceeds 20% levels. Maximum and minimum slip activities are observed in slip system 1 and slip system 4 as shown in Figure 3.14.

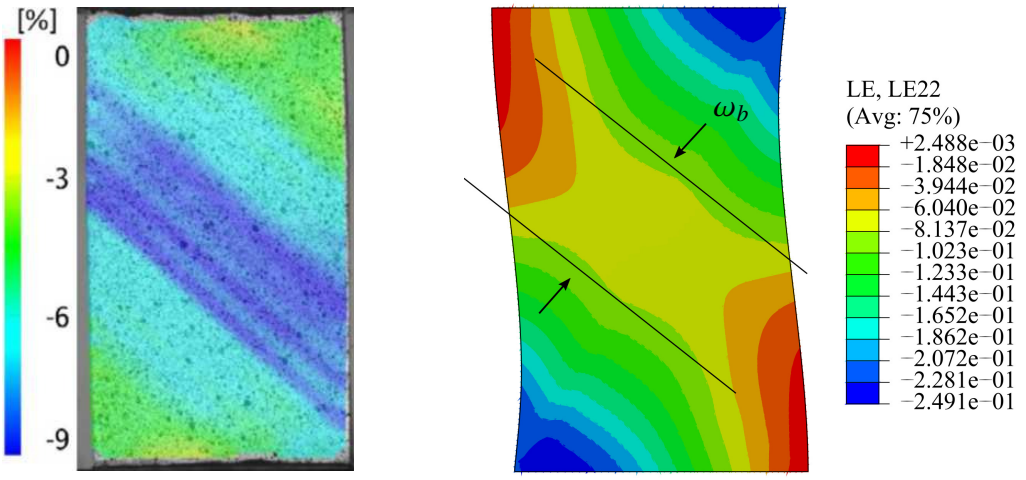

(a) (b)

Figure 3.13. (a) ϵ_{22} obtained by Digital Image Correlation (DIC) measurement device (b) ϵ_{22} contour of finite element analysis

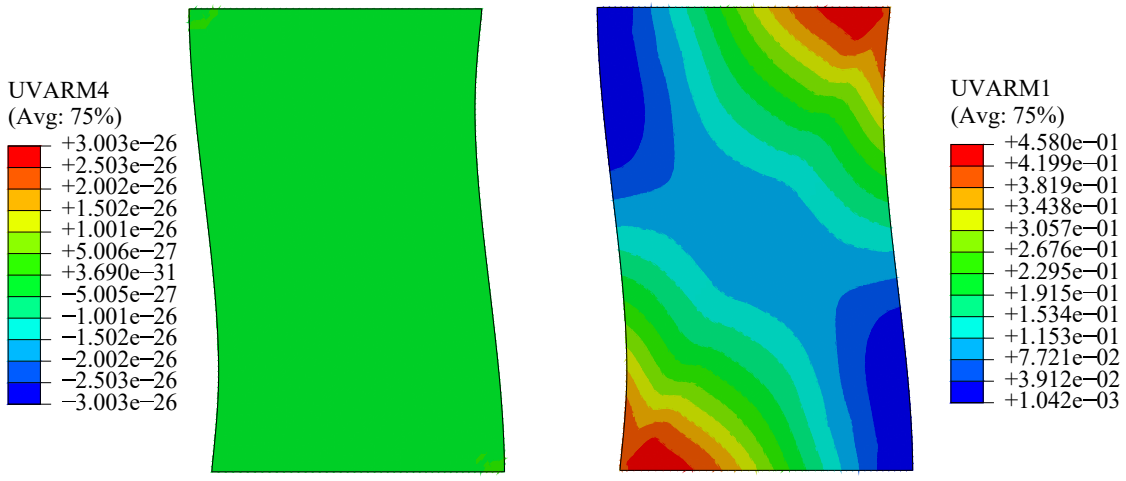

(a) (b)

Figure 3.14. (a) Minimum and maximum slip activities are observed in (a) slip system 4 and (b) slip system 1, respectively.

3.2.3. Compression Test on $\theta = 75°$ Specimen

In finite element model, degrees of freedoms at the bottom reference point is prescribed to zero whereas at the top a displacement of 0.32 mm is applied in y-direction. Considering loading rate in experiments, step time is defined as 40 sec for the given displacement.

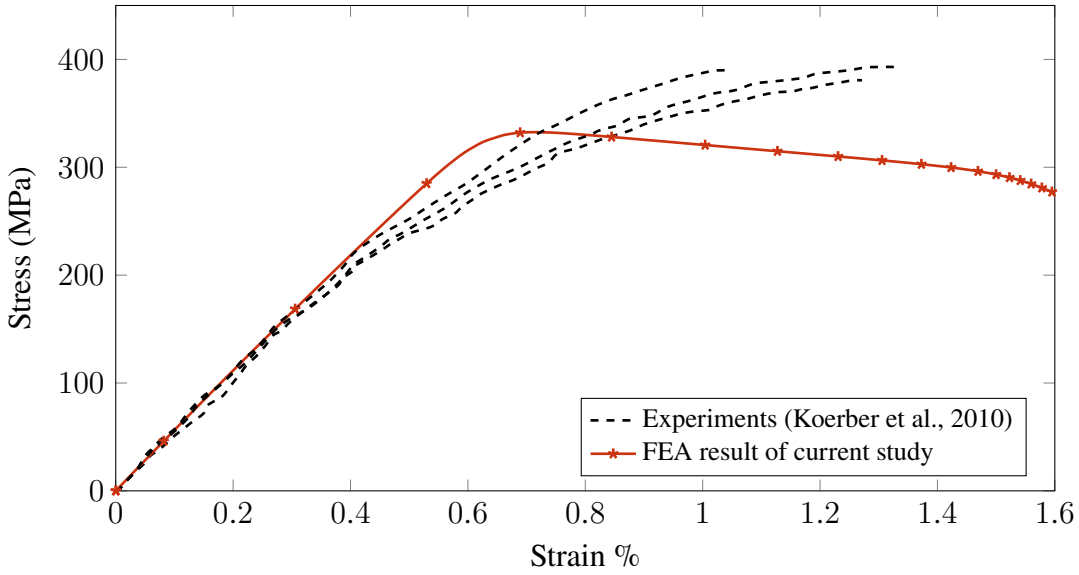

Figure 3.15. Comparison of simulation and the experimental results for $\theta = 75°$

Figure 3.15 illustrates the comparison of finite element analysis result with the experimental results for compression test of $[75°]_{32}$. Stress is calculated by dividing applied force on the cross-sectional area. In the case of $\theta = 75°$, a much higher stress value is obtained for 0.6% strain compared to other two cases. While the FEA estimation is consistent with the initial tangent obtained in the experimental results, a significant softening appears after 0.6% strain value. A huge amount of fibre rotations causes plastic micro-buckling (Budiansky & Fleck, 1993) and followed by fibre kinking obtained in Figure 3.17.

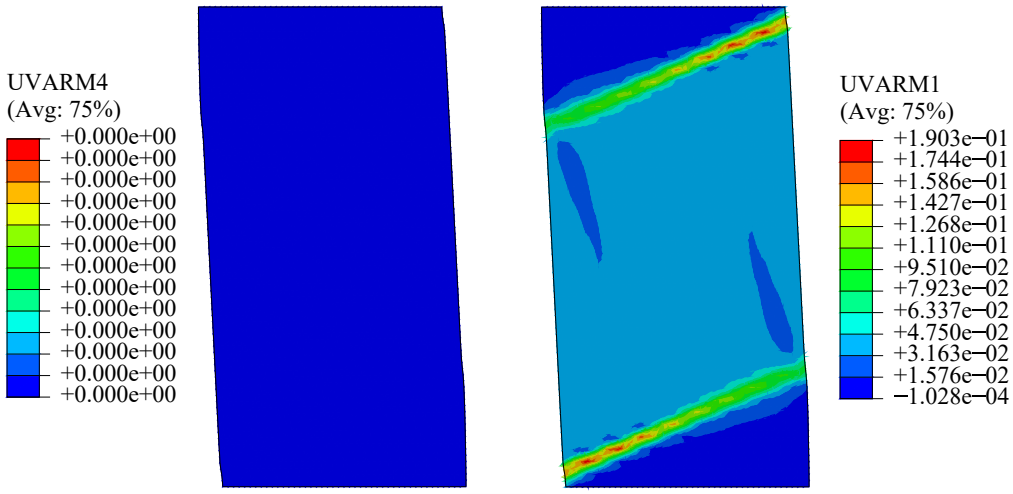

Figure 3.16. (a) There is no slip activitiy in slip system 1. (b) Maximum slip activities are observed in slip system 1.

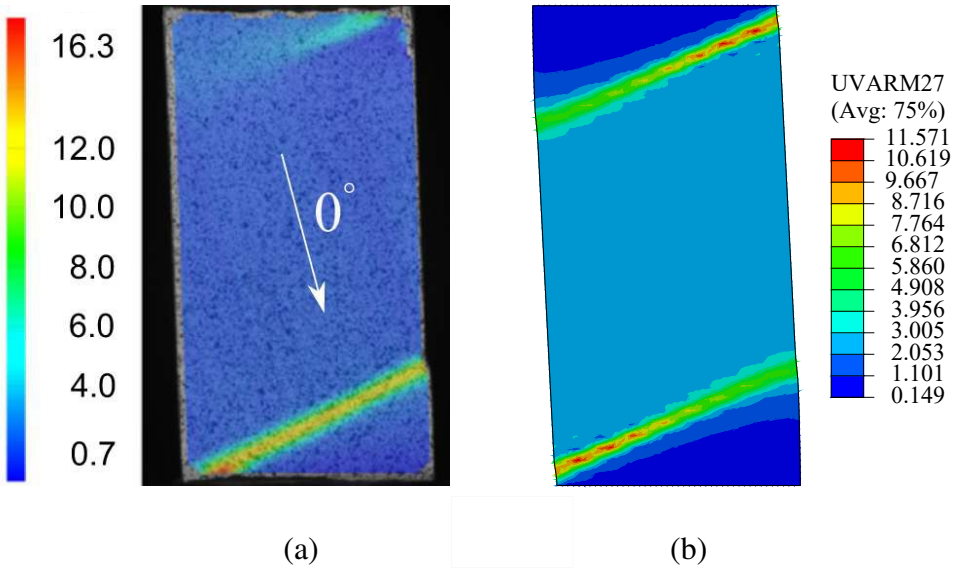

Figure 3.17. Comparison of DIC measurements with rotation angle prediction of finite element analysis.

3.3. Shear Test on Cross-Ply Laminates

In this section finite element predictions obtained for shear test on $[\pm 90^\circ]_{4s}$ unidirectional laminates are compared with experimental results (Tan & Falzon, 2016) in order to validate the model. The specimen dimensions are presented in Figure 3.18. It consists of 16 layers throughout the thickness, and the thickness of each layer is approximately 0.21 mm. Radius of notches located on long edges are equal to 1.3 mm. The loading rate is stated as 1 mm/min in the study of Tan and Falzon (2016). Displacement controlled experiments were conducted by using screw-driven mechanical testing machine. The specimen subjected to shear by clamping right and left parts to testing machine. It is mentioned that the surfaces of the specimen was roughened by sandpaper to hold specimen firmly. Engineering shear strain was calculated by summing logarithmic strains measured at two strain gauges those located in the direction of $\pm 45^\circ$. The approximate locations of the strain gauges are shown in Figure 3.18. The stacking orientation of the $[\pm 90^\circ]_{4s}$ cross-ply model is given in Figure 3.19a. Shear stresses were obtained by dividing the reaction force by the cross-sectional area of the narrowest section. In the calculation of the stress, the effect of notch radius hence stress concentration is neglected. The material parameters used in all shear analysis is presented in Table 3.3.

Table 3.3. Model Parameters for AS4/PEEK (Tan & Falzon, 2016)

Material Parameter	Value
E_f	138000 MPa
E_m	10300 MPa
τ_y	80.81 MPa
μ	0.28
ν_{12}	0.3
ν_{13}	0.3
ν_{23}	0.3
G_{12}	5200 MPa
m	0.045

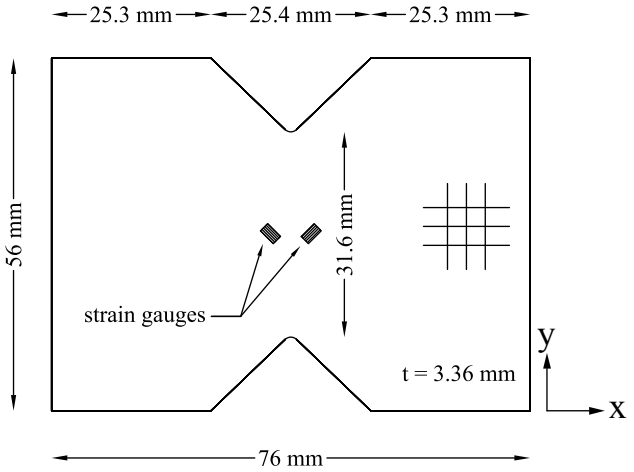

Figure 3.18. The geometry of $[\pm 90]_{4s}$ cross-ply model

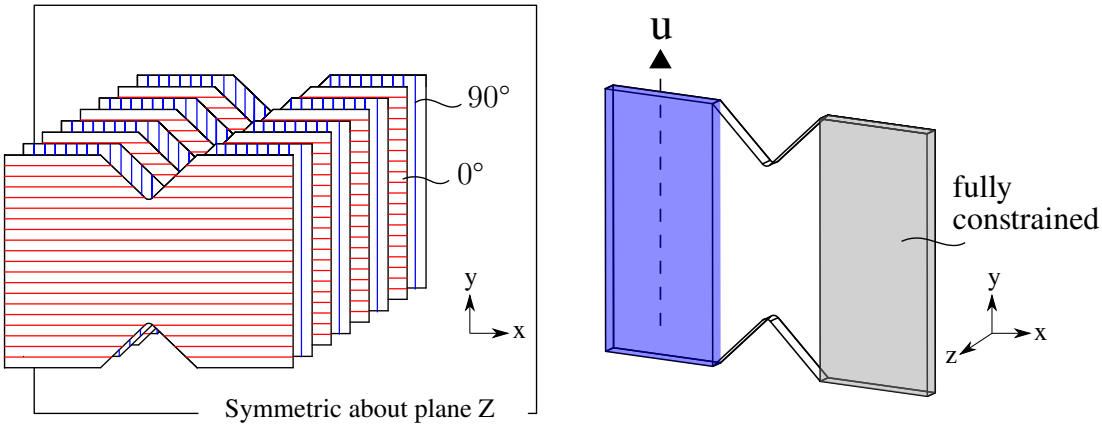

(a) (b)

Figure 3.19. (a) Stacking orientation of $[\pm 90]_{4s}$ cross-ply model (Fibres are depicted by dashed lines.). (b) Boundary conditions of finite element model is presented. A displacement is applied to left (blue) part in the direction of u and right (grey) part is fully constrained.

In the finite element analysis, the model is discretized by UEL which has the topology of twenty noded quadratic brick element and has eight integration points. The model is created symmetrically by utilizing the symmetry boundary conditions in the z-direction on the back surface. A displacement along y direction imposed to nodes at left part whereas nodes at the right part are fully constrained. Defined boundary conditions are illustrated in Figure 3.19b. Shear strain was calculated from the logarithmic strains at the nodes, which correspond approximately to the midpoints of strain gauge areas. To check mesh dependency and mesh convergence, the analysis is repeated for three different mesh densities, as shown in Figure 3.20. There is no remarkable difference between the responses of different element sizes. It shows that the analysis is mesh independent. For that reason, medium-size structured mesh is used for further analysis.

Figure 3.21 shows the comparison of predicted response, experimental results and finite element analysis result conducted by Tan and Falzon (2021). Stress-strain response can be considered in three different parts as linear part, plateau and hardening. The initial tangent of linear behaviour is consistent with Tan's simulation result and one of the experimental results. In the experimental results, the mild hardening seen in the plateau part is also obtained with the current model. It is worthy to note that eight-node brick elements with reduced integration points (C3D8R in the Abaqus notation) were used in the study of Tan and Falzon (2021). It can be concluded that the predicted behaviour has successfully experimental results up to 35% strain. Since the damage in the specimen is not taken into account in the model yet, excessive hardening is observed in higher strains.

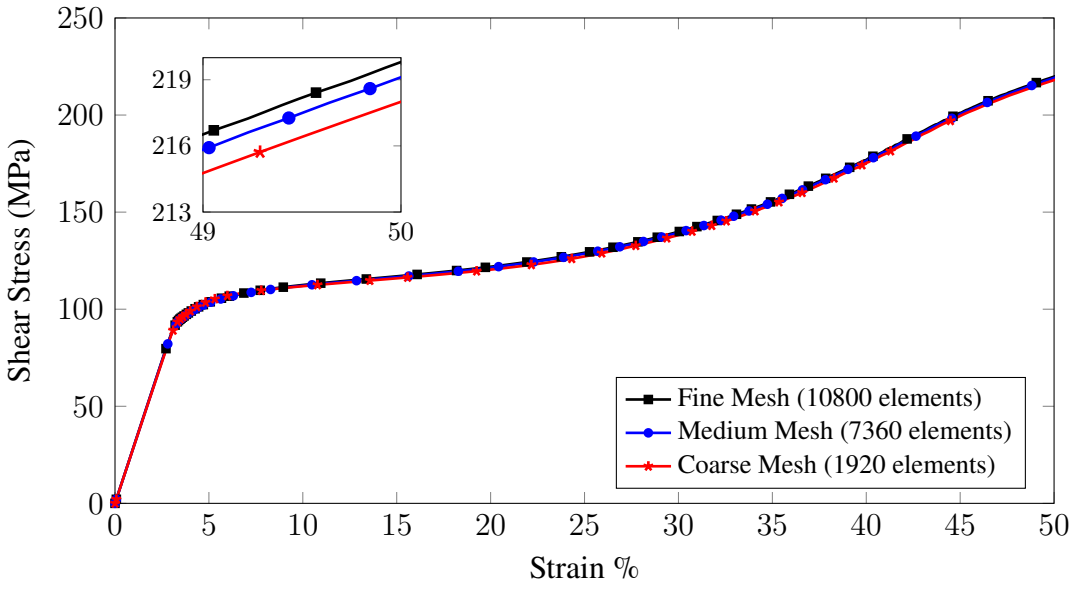

Figure 3.20. Mesh convergence of the cross-ply model is investigated by 3 different mesh densities.

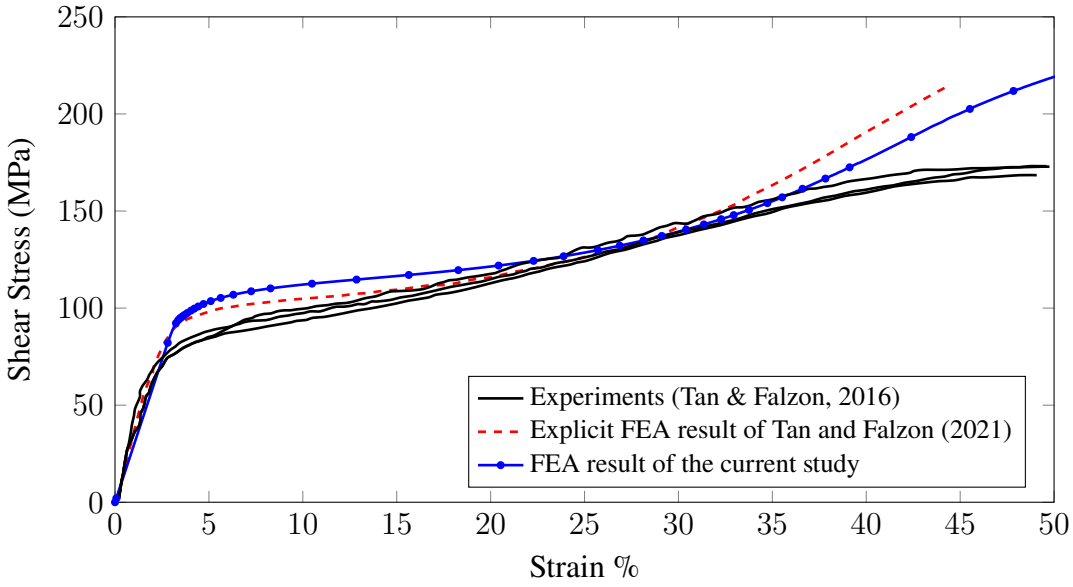

Figure 3.21. Comparison of simulation results with the experimental results for $[\pm 90°]_{4s}$ and prediction of Tan and Falzon (2021)

Produced shear strain distribution is compared to DIC measurements at $\gamma_{12} = 18\%$ in Figure 3.22. The shear strain contour matches the DIC measurements obtained during the experiment. As expected, the shear strain increases in the notched section which is named as fracture zone and decreases towards the edges of the model. Figure 3.23 shows comparison of predicted fibre rotation and measured fibre rotation in experiment. The

measured and predicted fibre rotation angles are 12° and 12.8°, respectively.

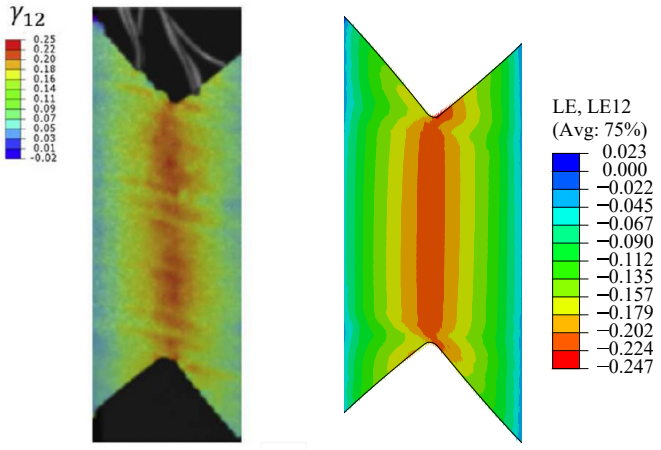

(a) (b)

Figure 3.22. Comparison of shear strain contours at 18% strain obtained from (a) DIC measurements (Tan & Falzon, 2016) and (b) simulation results of current study.

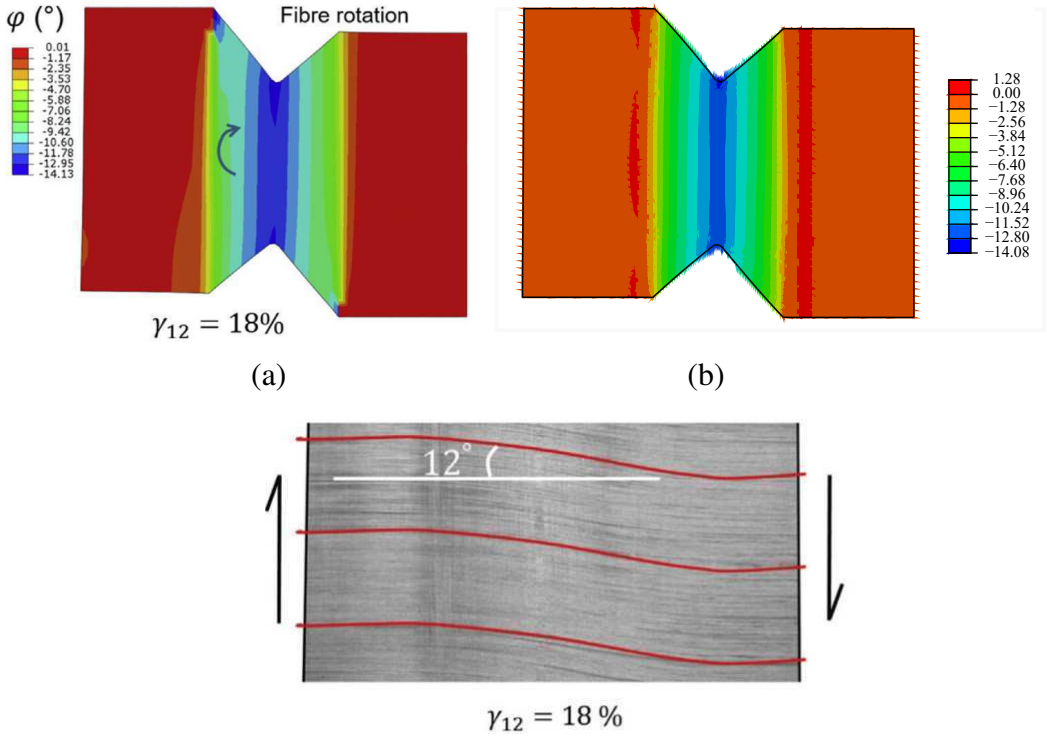

(a) (b)

(c)

Figure 3.23. Comparison of fibre rotation contours at 18% strain obtained from (a) prediction of Tan and Falzon (2021) and (b) simulation results of current study and (c) experimental observation by Tan and Falzon (2016).

3.4. Parametric Study on Cross-Ply Shear Analysis

A parametric study on cross-ply shear analysis provides an understanding of the sensitivity of material response to its model parameters. To this end, the influence of yield stress, rate sensitivity exponent, and friction coefficient on the behaviour of shear response is investigated in this section. While performing a parametric study for each parameter mentioned, the remaining material parameters were kept constant.

3.4.1. Influence of Yield Stress

Stress-strain response of the material AS4/PEEK with different yield stresses for $[\pm 90^\circ]_{4s}$ is presented in Figure 3.24. In all three cases, as expected, the initial tangent demonstrates the same characteristics until the yield point. Increasing yield stress affects the stress level of the plateau. So, the analysis with larger yield stress produces the highest ultimate stress among the three analyses. Considering the three different analyses, the differences in yield value did not cause any change in the overall behaviour.

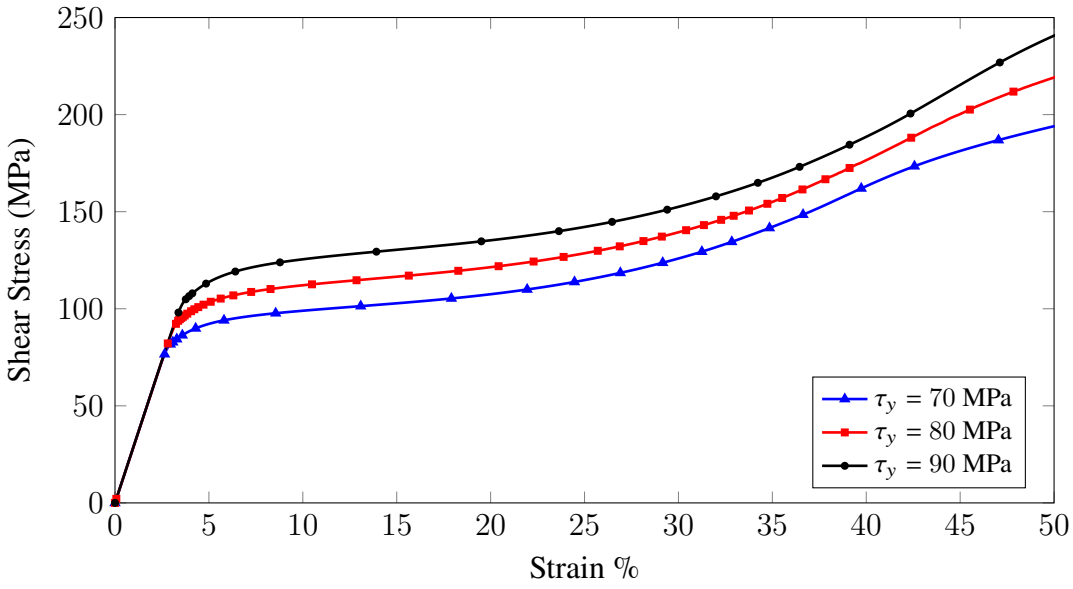

Figure 3.24. Comparison of simulation results produced from $[\pm 90^\circ]_{4s}$ model for different yield stress values

3.4.2. Influence of Rate Sensitivity Exponent

Stress-strain response of the material AS4/PEEK with different rate sensitivity exponents for $[\pm 90^\circ]_{4s}$ is presented in Figure 3.25. Parametric study for various rate sensitivity is much more complex compared to yield stress. There is a slight difference in initial tangent which effects the beginning strain plateau. An increase in the value of m causes a growth in elastic strains, and therefore a decrease in plastic strains. For that reason higher rate sensitivity exponent leads to larger stress value for the same strain value.

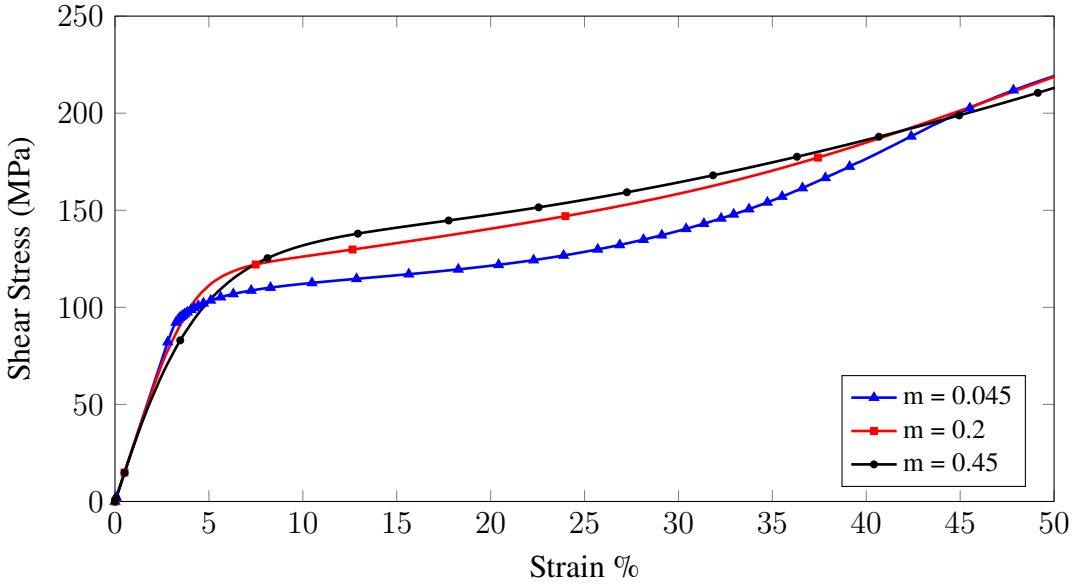

Figure 3.25. Comparison of simulation results produced from $[\pm 90^\circ]_{4s}$ model for different rate sensitivity exponent values

3.4.3. Influence of Friction Coefficient

Stress-strain response of the material AS4/PEEK with different friction coefficient for $[\pm 90^\circ]_{4s}$ are presented in Figure 3.26. While different friction values does not cause any change up to 18% strain, higher friction coefficient leads to higher stresses at larger strain levels. As it is stated in Equation 2.20, the hardening mechanism in the model is controlled by the pressure. Therefore, hardening response depends on stress state. An increase in the friction coefficient triggers the hardening mechanism and leads to an increase in the resistance of slip systems.

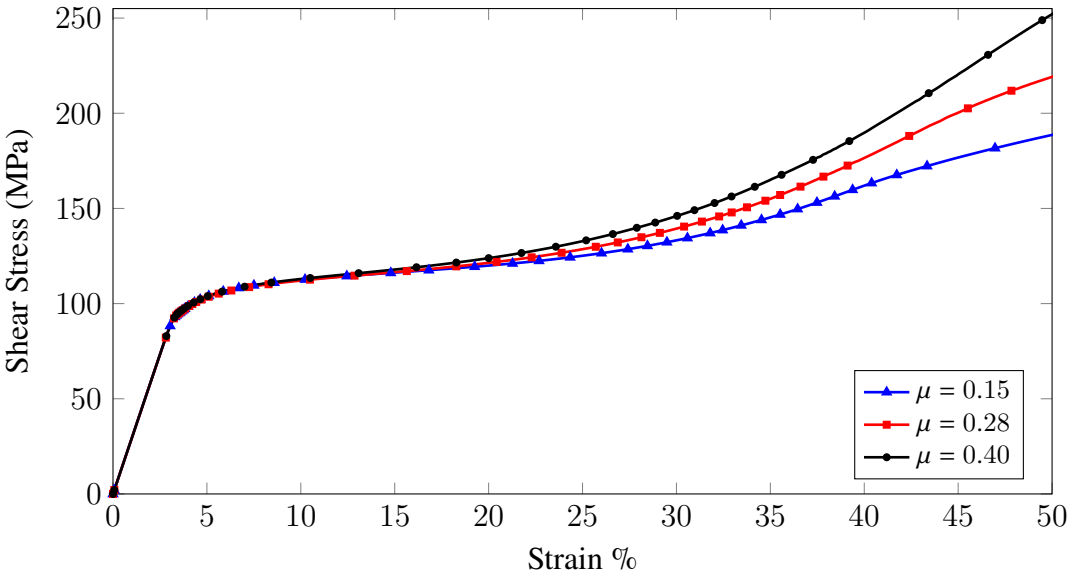

Figure 3.26. Comparison of simulation results produced from $[\pm 90^\circ]_{4s}$ model for different friction coefficient values

CHAPTER 4

INCORPORATION OF DAMAGE MECHANISMS

4.1. Introduction

Referring to Figure 4.1, finite element analysis predictions deviate from the experimental results at high strain levels, e.g. strain levels larger than %35. At these strain levels, it is expected that damage mechanisms would be activated and the mechanical properties of the material would deteriorate.

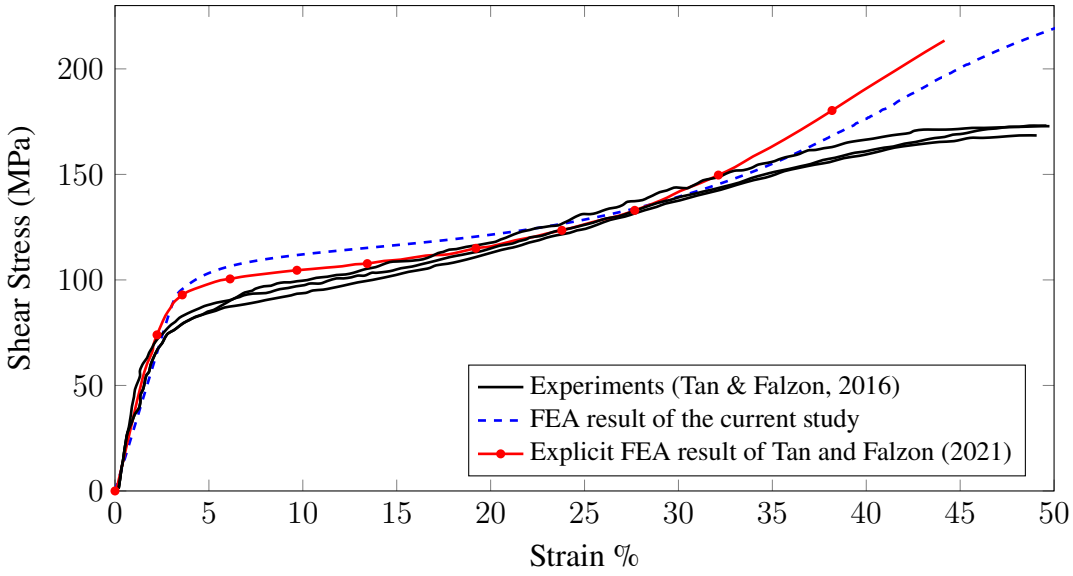

Figure 4.1. Comparison of simulation results with the experimental results for $[\pm 90^\circ]_{4s}$ (Tan & Falzon, 2016)

If the material micro-structure is recalled, it is composed of fibres embedded into a relatively ductile matrix. Matrix and the fibre-matrix interface are not free of flaws, e.g. micro-voids. The voids would enlarge and might coalesce, see Figure 4.2. Therefore, it is expected both resistance mechanism against slip and elastic properties would diminish.

In this chapter, the intention is to embed such micro-structural damage mechanisms into the continuum scale material model presented in previous chapters. To this end, continuum damage mechanics is going to be used where all micro-mechanical degradation

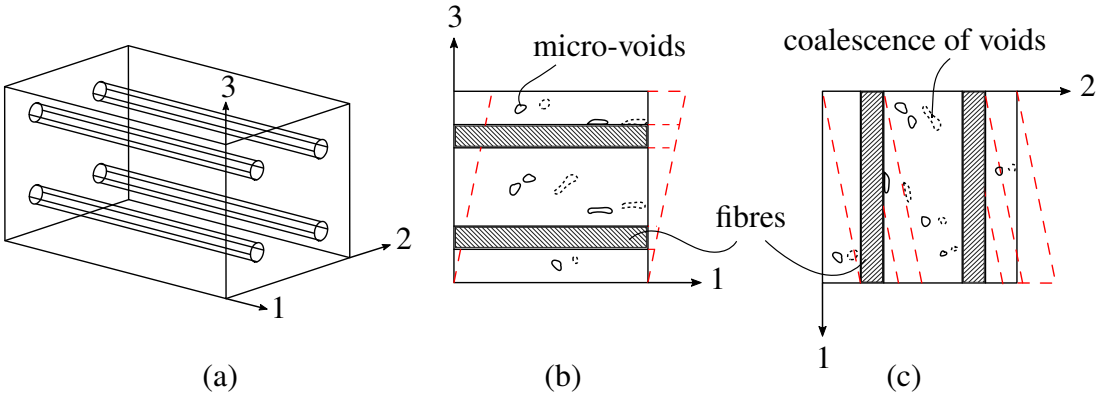

Figure 4.2. (a) Fibre direction coincides with dir-1. Illustrations for physical meaning of (b) G_{13} and (c) G_{12} are presented. Deformed shapes are depicted by dashed lines.

mechanisms are lumped in a damage variable D.

Referring back to Figure 4.1, at strain levels larger than 35%, a very large fraction of the strain is plastic. Therefore it is reasonable to correlate damage to plastic strains. However, there are two types of slip systems. For this reason, it makes sense to introduce two damage variables D^L and D^T associated with longitudinal and transverse slip systems, respectively. As these micro-mechanisms evolve, it is expected that resistance against slip would get weaker. Relying on this argument, resistance of undamaged material against slip (τ_y) and hardening term (μp) are both pre-multiplied by $(1 - D^p)$ where $p = L, T$ and $D^p \geq 0 \;\; \& \;\; D^p \leq 1.0$.

As far as elastic material properties are concerned, aforementioned damage mechanisms would effect them as well. Expecting change in the elastic material properties is inevitable when the damage is clearly visible. For that reason, some of the material properties are degraded depending on the damage variables during the analysis. Longitudinal and transverse modulus of elasticity parameters are scaled down by $(1 - D^L)$ and $(1 - D^T)$, respectively. In the same context, G_{12} and G_{13} are reduced by $(1 - D^T)$ and $(1 - D^L)$, respectively. Since the material is transversely isotropic, G_{23} is calculated by $(0.5\,E_m)/(1 + \nu_{23})$ with the degraded material parameters. It is assumed that there is no damage-related change in ν values.

4.2. Definition and Evolution of Damage Variables

As mentioned in the previous section, damage variables D^L and D^T are driven by plastic strain. To specify these variables explicitly, it is necessary to introduce history variables Γ^L and Γ^T. The specific form of Γ^L and Γ^T are defined as

$$\dot{\Gamma}^L = \sum_{m=1}^{3} |\dot{\gamma}_m|$$
$$\dot{\Gamma}^T = \sum_{m=4}^{6} |\dot{\gamma}_m| \tag{4.1}$$

Since damage is a non-decreasing process, history variables κ^L and κ^T are introduced as

$$\kappa^L = \max\left(\Gamma^L(\tau)\right) \qquad \tau \leq t$$
$$\kappa^T = \max\left(\Gamma^T(\tau)\right) \qquad \tau \leq t \tag{4.2}$$

where τ is time-like parameter describing the loading process until time t. For damage evolution, the following exponential form

$$D^p = 1 - \frac{\kappa_o^p}{\kappa^p}\left(1 - \alpha^p + \alpha^p e^{-\beta^p(\kappa^p - \kappa_o^p)}\right) \qquad p = \{L, T\} \tag{4.3}$$

is used where κ_o^p, α^p and β^p are fitting parameters. κ_o^p is the parameter that defines where damage starts to evolve in the model. Parameter α prevents the damage variable from reaching 1.0. β controls the rate of damage evolution, such that higher β values cause faster damage evolution. D - κ response of the exponential softening law is given in Figure 4.3.

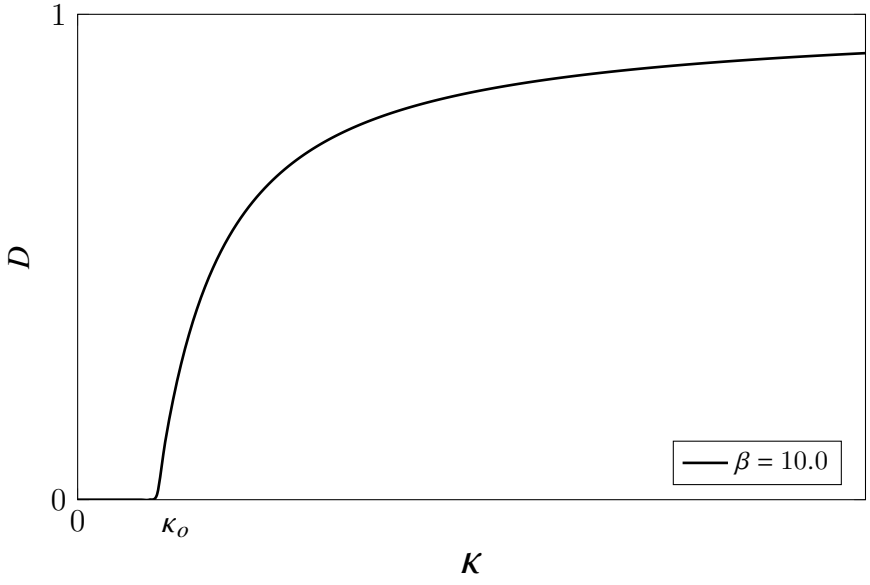

Figure 4.3. D - κ response of the exponential softening.

4.3. Temporal and Spatial Discretization

Equation 4.1 has to be converted into discrete form. Replacing $\dot{\Gamma}$ by $\left(\Gamma_{n+1}-\Gamma_n\right)/\Delta t$ and $|\dot{\gamma}_m|$ by $|\Delta\gamma|/\Delta t$, Equation 4.1 can be written as,

$$\Gamma^p_{n+1} = \begin{cases} \Gamma^L_n + \sum\limits_{m=1}^{3} |\Delta\gamma_m| & p = L \\ \Gamma^T_n + \sum\limits_{m=4}^{6} |\Delta\gamma_m| & p = T \end{cases} \tag{4.4}$$

Once Γ^p_{n+1} values are calculated, κ^L_{n+1}, κ^T_{n+1} and the damage variables D^L_{n+1} and D^T_{n+1} can be evaluated by following Algorithm 3 given on the next page. Since longitudinal and transverse damage parameters are functions of slip increments, linearization of the damage extended model would become cumbersome. Instead, taking the advantage of small time steps, a staggered algorithm is used such that damage variables are assumed to be frozen from t_n to t_{n+1} and they are updated at the end of each increment; at t_{n+1}. Therefore, resistances on slip system η at t_{n+1} are calculated as

$$g^\eta_{n+1} = \begin{cases} (1 - D^L_n)(\tau_y + \mu\, p) & \eta = 1, 2, 3 \\ (1 - D^T_n)(\tau_y + \mu\, p) & \eta = 4, 5, 6 \end{cases} \tag{4.5}$$

where D^L_n and D^T_n are damage parameters available from the previous step t_n. Similarly, D^L_n and D^T_n are used to reduce the elastic material properties. General structure of the procedure for the incorporation of damage mechanism is given in Algorithm 3. In the next section, cross-ply shear test is reconsidered using the damage extended model.

Algorithm 3 Algorithm of Damage Extended Model

Available: D_n^T & D_n^L –from the previous step.

Start increment

Solve Local N-R with the previous damage parameter (multiply resistance components by $(1 - D_n^T)$ and $(1 - D_n^L)$ according slip system classification & degrade material parameters),

Conclude Local N-R

Update Γ_{n+1}^T & Γ_{n+1}^L,

$$\Gamma_{n+1}^L = \Gamma_n^L + \sum_{m=1}^{3} |\Delta\gamma_m| \quad \& \quad \Gamma_{n+1}^T = \Gamma_n^T + \sum_{m=4}^{6} |\Delta\gamma_m|$$

Calculate κ^T & κ^L

if $\Gamma_{n+1}^T < \kappa_n^T$ **then**

$\kappa_{n+1}^T \leftarrow \Gamma_{n+1}^T$

else

$\kappa_{n+1}^T \leftarrow \kappa_n^T$

end if

if $\Gamma_{n+1}^L < \kappa_n^L$ **then**

$\kappa_{n+1}^L \leftarrow \Gamma_{n+1}^L$

else

$\kappa_{n+1}^L \leftarrow \kappa_n^L$

end if

Calculate D_{n+1}^T & D_{n+1}^L

if $\kappa_{n+1}^L < \kappa_o^L$ **then**

$D_{n+1}^L \leftarrow 0$

else

$D_{n+1}^L \leftarrow 1 - \left(\kappa_o^L / \kappa_{n+1}^L\right)\left(1 - \alpha^L + \alpha^L e^{-\beta^L\left(\kappa_{n+1}^L - \kappa_o^L\right)}\right)$

end if

if $\kappa_{n+1}^T < \kappa_o^T$ **then**

$D_{n+1}^T \leftarrow 0$

else

$D_{n+1}^T \leftarrow 1 - \left(\kappa_o^T / \kappa_{n+1}^T\right)\left(1 - \alpha^T + \alpha^T e^{-\beta^T\left(\kappa_{n+1}^T - \kappa_o^T\right)}\right)$

end if

End of the increment

Update damage variables, store them as history variables

$$D_n^L \leftarrow D_{n+1}^L \quad \& \quad D_n^T \leftarrow D_{n+1}^T$$

4.4. Cross-Ply Shear Test

Cross-ply shear test considered in Section 3.3 is re-analysed using the damage extended model presented in this chapter. Material and damage model parameters are given in Table 4.1.

Table 4.1. Material and damage parameters used in damage extended model.

Material Parameter	Value
E_f	138000 MPa
E_m	10300 MPa
τ_y	80.81 MPa
μ	0.28
ν_{12}	0.3
ν_{13}	0.3
ν_{23}	0.3
G_{12}	5200 MPa
m	0.045
κ_o	0.017
α	0.1
β	100

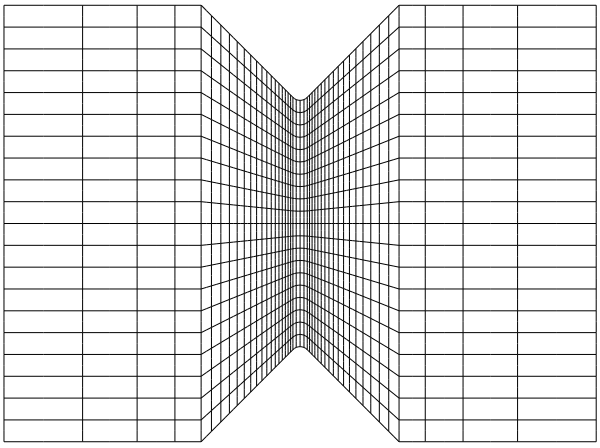

Figure 4.4. Fine mesh for $[\pm 90]_{4s}$ Cross-ply Model

The resulting slip distributions obtained by the original model (without damage) for the most active slip systems in two classes at 50% strain level are shown in Figure 4.5 side by side. It indicates that obtained slips in longitudinal systems are relatively large compared to those in transverse systems. Therefore, the damage in longitudinal systems is expected to be larger than the damage in transverse systems. For this reason, the fitting parameters of D^L were determined first and these values were taken as valid for the fitting parameters of D^T. Similar to the previous chapters, twenty-noded quadratic brick elements are used to discretize the model. Two variants of twenty-noded brick element with 8 and 27 integration points are considered.

Preliminary analysis with 8 integration points shows that an instability (probably a numerical instability similar to hour-glassing) is observed, please see Figure 4.6. However, when 27 integration points are used, these instabilities disappear as shown on the right-hand side of Figure 4.6. Therefore, 27 integration points are used for the analysis presented in this chapter.

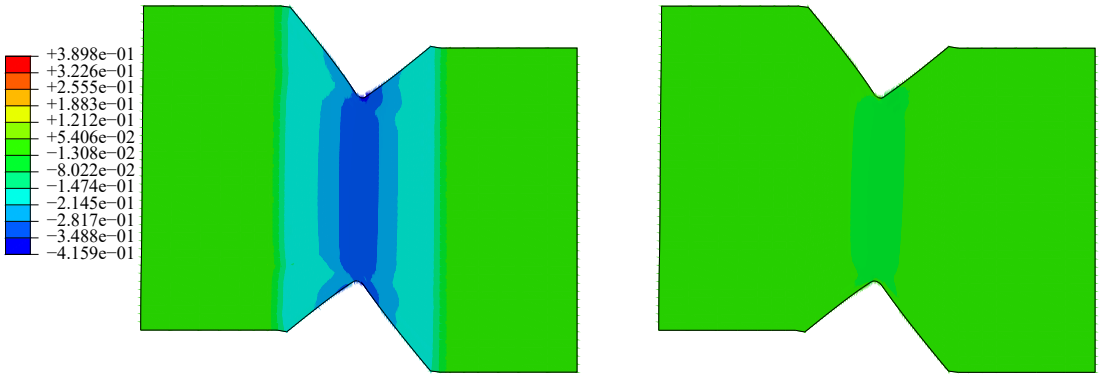

Figure 4.5. Slip distribution contours of without damage model for longitudinal slip system-1 (left side), transverse slip system-6 at 50% strain level (right side). These two slip systems are the most active ones in their classes.

An important issue in damage mechanics is mesh dependency and mesh convergence. One of the methods to mitigate mesh dependency problem is to insert rate dependency in the model. Since the discussed model is already rate dependent, no significant mesh dependency is expected. To verify this, the analysis is repeated for 3 times by increasing mesh densities on the centre of the model. Corresponding stress-strain responses are presented in Figure 4.7. Coarse, medium and fine meshes correspond to 1024, 4160 and 7360 elements, respectively. The constructed fine mesh is shown in Figure 4.4. The comparison indicates that there is no mesh dependency in the problem.

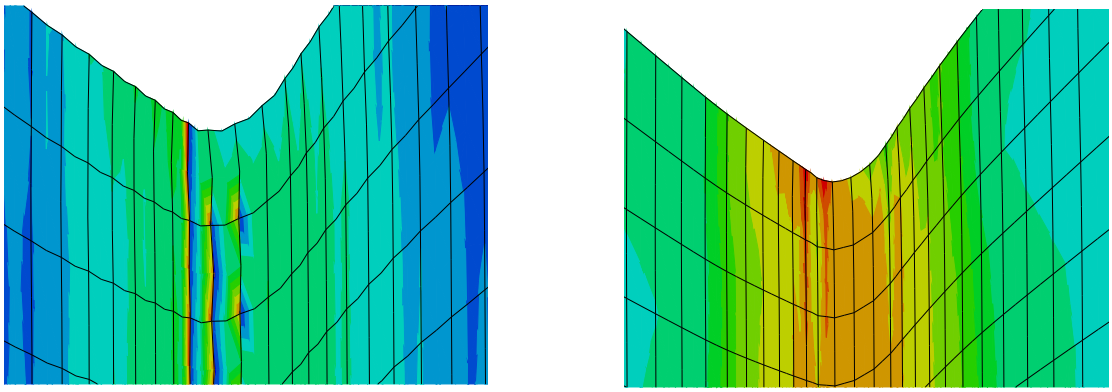

(a) (b)

Figure 4.6. (a) Instabilities are observed when using 8-integration points, (b) instabilities have disappeared when using 27-point integration (strain level is 37% for both cases).

Figure 4.8 shows the contour plot of D^L and D^T at %50 shear strain level. There is no damage in transverse slip systems since κ^T is smaller than the threshold κ_0^T which is set

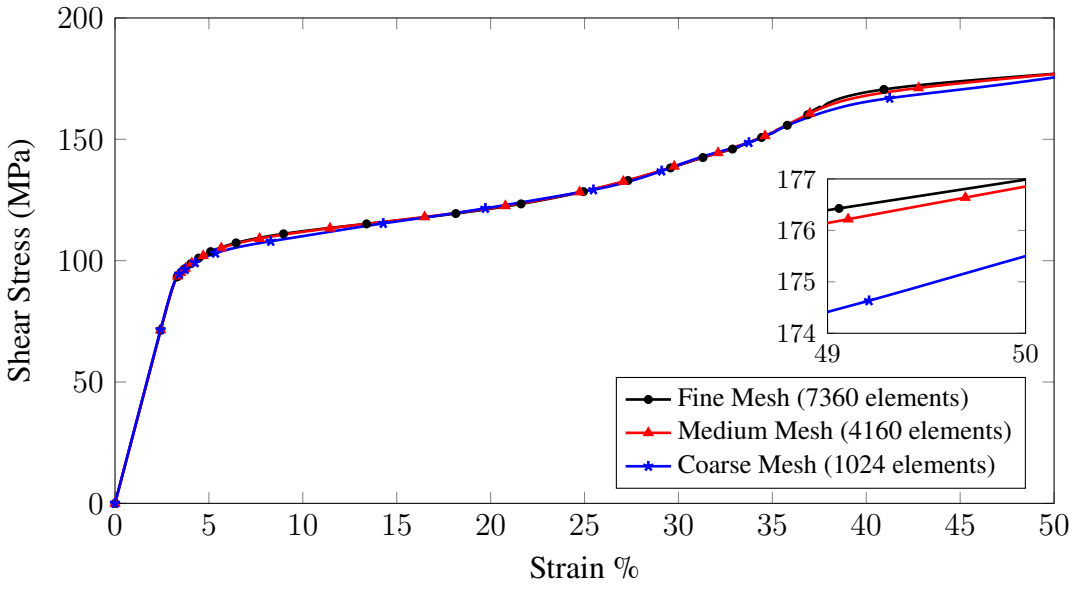

Figure 4.7. Comparison of damage extended simulation results for different mesh densities.

equal to κ_0^L. Obviously, the damage is concentrated in the centre of the specimen and more around the notch than in the other parts. In Figure 4.9, experimental results are compared to the original predictions (without damage) and damage extended models. It is clear that the deviations between experimental results and finite elements predictions without damage beyond approximately 35% strain levels is overcome by the damage extended model.

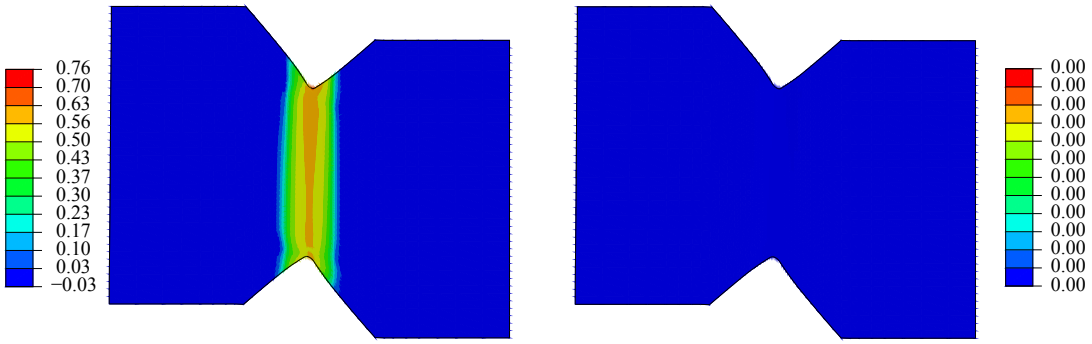

(a) (b)

Figure 4.8. Contour of damage in (a) longitudinal and (b) transverse slip systems at $\gamma_{12} = 50\%$.

Especially in the top-notch region, compressive normal stresses occur under shear loading. Hence local compressive stresses might trigger local instabilities. In order to

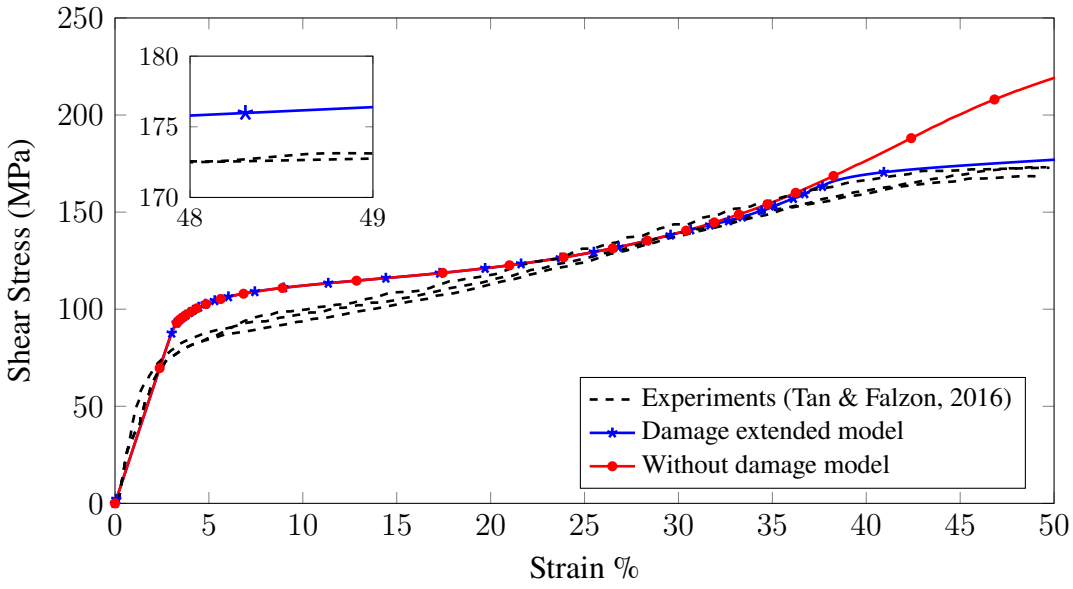

Figure 4.9. Comparison of damage extended simulation results with the model without damage.

investigate this, the symmetry boundary conditions on the back face of the model were removed. Thus, a thinner and therefore more slender specimen is observed. The deformed configuration obtained at approximately 90% strain levels as a result of the analysis is shown in Figure 4.10a. An inclined instability band through the thickness direction is clearly visible in the notch region. The fibre rotation angle obtained at this strain level is also shown in the Figure 4.10b. The large fibre rotation angle differences between the adjacent plies indicate that the probability of interlayer damage is significant. Therefore, it seems that a failure process in which both delamination and fibre local buckling evolves in a combined manner is quite possible.

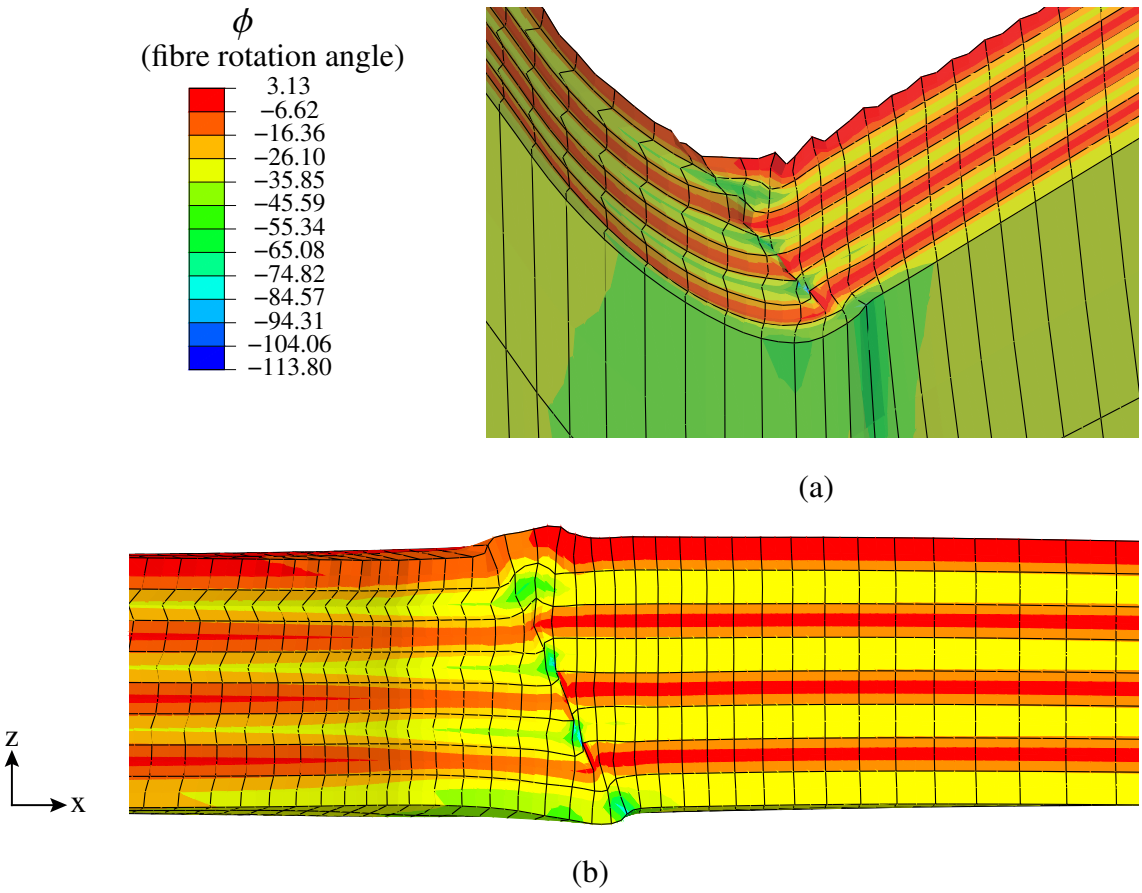

Figure 4.10. (a) Local instabilities are observed at notch region (perspective view). (b) There is large fibre rotation angle difference between the adjacent plies (top view).

CHAPTER 5

CONCLUSION & OUTLOOK

5.1. Summary & Main Findings

In this thesis, a recently proposed material model for elastoplastic response of fibre reinforced composites is re-considered and implemented in an implicit finite element solution framework. The model is inspired by crystal plasticity and, so far, was elaborated for an explicit finite element algorithm. In this work, the model is recast in implicit form and implemented in commercial finite element software Abaqus through user-defined element subroutine (UEL).

In Chapter 3, three different cases have been considered to validate the model. Firstly, the stress update algorithm was verified with the analytical solution derived for the simple shear case. The numerical results obtained for two different fibre orientations, 0° and 90°, are consistent with the analytical solutions. In addition, the behaviour beyond the yielding point is affected by fibres which may cause a hardening mechanism according to fibre orientation. Afterwards, the limits of the model were pushed by considering compression and cross-ply shear tests reported in the literature. Contrary to the success of the model in cross-ply shear test, the stress-strain responses obtained in the compression tests show some differences compared to experimental results. It is worthy to note that in case of both cross-ply shear test and 45° compression test the matrix plasticity is activated and relatively larger strain levels are reached. Therefore, it is concluded that the model produces more accurate results in case of significant matrix plasticity. Referring back to cross-ply shear test, the numerical predictions of the model are promising up to approximately 35% strain level. Contrary to the experimental results, an excessive hardening was observed in the finite element predictions at high strains. At these deformation levels, matrix and matrix-fibre interface damages are inevitable.

To remedy this discrepancy, in Chapter 4, the model is extended with a continuum scale damage model. It is aimed to mitigate the deviation observed in shear analyses conducted in Chapter 3 at high strains. According to the slip system classification, the damage is lumped in two different damage parameters. The intention is to suppress the

excessive hardening by degrading the resistance to slip and the elastic material parameters. The proposed model is affordable in terms of time and computational power. However, this is a phenomenological approach, and some weaknesses are obvious. The shear strain level at which the damage evolution starts and the parameters that drive the evolution law are determined by curve fitting. The damage evolution law has almost no relation to the micro-mechanism of damage initiation and growth. However, micro-mechanical damage models are beyond the scope of this thesis. Shear test was re-analyzed with damage extended model, and the deviation between finite element predictions and experimental results for strain levels larger than 35% almost disappeared. The main findings of the thesis can be summarized as follows:

- The predictions of compression analyses for 45° and 75° are not satisfactory considering strain contour and stress-strain response comparisons.
- The prediction of shear analysis for cross-ply model is satisfactory up to %35 strain levels.
- Based on the observations mentioned in the previous two items, the proposed model produces better results when the matrix plasticity is dominant. Therefore, more accurate predictions are obtained in case of matrix exposed to shear loading.
- By incorporating damage to the model, the deviation beyond %35 strain level is overcome. The damage extended model is feasible in terms of computational power. However, it is a phenomenological approach that does not reflect the micro-mechanical damage mechanisms.

5.2. Recommendations for Future Works

The study presented in this thesis can be improved and extended in a number of ways.

- For the crystal plasticity inspired modelling of composites, the choice of slip systems is not as straightforward as the slip systems in metal crystal plasticity. In the literature, several different slip angles are presented that define slip systems based on different motivations, such as fibre arrangement and capturing of yield point. It seems that determination of slip angles for composites is an unsolved problem and requires further investigation.

- Composites formed by fibre and matrix materials may have inherent defects like micro-voids. Under loading, these micro-voids can expand and even coalesce between adjacent spaces. The identification of these micro-voids requires approaches at the micromechanical level. Damage studies at the micromechanical level on composite structures can provide damage models with a more robust physical background.

- Delamination is one of the dominant damage modes encountered in experimental studies on composite elements under certain loading conditions. As described in Chapter 4, large variation of fibre angle rotation from ply to ply might trigger delamination around the notch region. Therefore, the current study can be extended to capture delamination failure by using cohesive interface elements between the plies.

- Referring back to Figure 1.1, ductile behaviour similar to metallic materials can be obtained by combining differently oriented thin plies. Achieving ductility by reducing the ply thickness and stacking different plies presents an interesting optimization problem.

REFERENCES

ABAQUS/Standard. (n.d.). *User's manual, version 6.14*. Dassault Systèmes.

Bathe, K. (2006). *Finite element procedures*. Prentice Hall. https://books.google.com.tr/books?id=rWvefGICfO8C

Bonet, J., & Wood, R. D. (2008). *Nonlinear continuum mechanics for finite element analysis* (2nd ed.). Cambridge University Press. https://doi.org/10.1017/CBO9780511755446

Budiansky, B., & Fleck, N. (1993). Compressive failure of fibre composites. *Journal of the Mechanics and Physics of Solids*, *41*(1), 183–211. https://doi.org/10.1016/0022-5096(93)90068-Q

de Souza Neto, E., Peric, D., & Owen, D. (2011). *Computational methods for plasticity: Theory and applications*. Wiley. https://books.google.com.tr/books?id=21Q0oLGFZuoC

Ekh, M., Lillbacka, R., & Runesson, K. (2004). A model framework for anisotropic damage coupled to crystal (visco)plasticity. *International Journal of Plasticity*, *20*(12), 2143–2159. https://doi.org/10.1016/j.ijplas.2004.04.007

Frossard, G., Cugnoni, J., Gmür, T., & Botsis, J. (2016). Mode i interlaminar fracture of carbon epoxy laminates: Effects of ply thickness. *Composites Part A: Applied Science and Manufacturing*, *91*, 1–8. https://doi.org/10.1016/j.compositesa.2016.09.009

Fuller, J., & Wisnom, M. (2015). Pseudo-ductility and damage suppression in thin ply cfrp angle-ply laminates. *Composites Part A: Applied Science and Manufacturing*, *69*, 64–71. https://doi.org/10.1016/j.compositesa.2014.11.004

Fuller, J., & Wisnom, M. (2018). Ductility and pseudo-ductility of thin ply angle-ply cfrp laminates under quasi-static cyclic loading. *Composites Part A: Applied Science and Manufacturing*, *107*, 31–38. https://doi.org/10.1016/j.compositesa.2017.12.020

Hinton, M., Kaddour, A., & Soden, P. (2002). A comparison of the predictive capabilities of current failure theories for composite laminates, judged against experimental evidence. *Composites Science and Technology*, *62*(12), 1725–1797. https://doi.org/10.1016/S0266-3538(02)00125-2

Kaddour, A., & Hinton, M. (2013). Maturity of 3d failure criteria for fibre-reinforced composites: Comparison between theories and experiments: Part b of WWFE-II.

Journal of Composite Materials, *47*(6-7), 925–966. https://doi.org/10.1177/0021998313478710

Koerber, H., Xavier, J., & Camanho, P. (2010). High strain rate characterisation of unidirectional carbon-epoxy im7-8552 in transverse compression and in-plane shear using digital image correlation. *Mechanics of Materials*, *42*(11), 1004–1019. https://doi.org/10.1016/j.mechmat.2010.09.003

Larsson, R., Singh, V., Olsson, R., & Marklund, E. (2022). A micromechanically based model for dynamic damage evolution in unidirectional composites. *International Journal of Solids and Structures*, *238*, 111368. https://doi.org/10.1016/j.ijsolstr.2021.111368

Lu, F., Guang, Z., Ke-shi, Z., Xu, J. Q., & Hai-dong, Y. (2004). On analysis of the elasto-viscoplastic response of single crystals with anisotropic damage: Constitutive modelling and computational aspects. *International Journal for Numerical Methods in Engineering*, *61*(3), 406–432. https://doi.org/10.1002/nme.1072

Luo, C., & Chattopadhyay, A. (2011). Prediction of fatigue crack initial stage based on a multiscale damage criterion. *International Journal of Fatigue*, *33*(3), 403–413. https://doi.org/10.1016/j.ijfatigue.2010.09.014

Mandel, U., Taubert, R., & Hinterhölzl, R. (2015). Mechanism based nonlinear constitutive model for composite laminates subjected to large deformations. *Composite Structures*, *132*, 98–108. https://doi.org/10.1016/j.compstruct.2015.04.029

Meza, L. R., Schormans, J. M., Remmers, J. J., & Deshpande, V. S. (2019). Shear response of 3d non-woven carbon fibre reinforced composites. *Journal of the Mechanics and Physics of Solids*, *125*, 276–297. https://doi.org/10.1016/j.jmps.2018.12.019

Nemat-Nasser, S., Hori, M., & Achenbach, J. (2013). *Micromechanics: Overall properties of heterogeneous materials*. Elsevier Science. https://books.google.com.tr/books?id=wm8vBQAAQBAJ

Ogihara, S., & Nakatani, H. (2012). Effect of ply thickness on mechanical property of cfrp symmetric angle-ply laminates. *Proceedings of ECCM-15*.

Potirniche, G., Horstemeyer, M., & Ling, X. (2007). An internal state variable damage model in crystal plasticity. *Mechanics of Materials*, *39*, 941–952. https://doi.org/10.1016/j.mechmat.2007.04.004

Saito, H., Morita, M., Kawabe, K., Kanesaki, M., Takeuchi, H., Tanaka, M., & Kimpara, I. (2011). Effect of ply-thickness on impact damage morphology in cfrp laminates. *Journal of Reinforced Plastics and Composites*, *30*(13), 1097–1106. https://doi.org/10.1177/0731684411416532

Tan, W., & Falzon, B. G. (2016). Modelling the nonlinear behaviour and fracture process of as4/pekk thermoplastic composite under shear loading. *Composites Science and Technology*, *126*, 60–77. https://doi.org/10.1016/j.compscitech.2016.02.008

Tan, W., & Falzon, B. G. (2021). A crystal plasticity phenomenological model to capture the non-linear shear response of carbon fibre reinforced composites. *International Journal of Lightweight Materials and Manufacture*, *4*(1), 99–109. https://doi.org/10.1016/j.ijlmm.2020.06.004

Tan, W., & Liu, B. (2020). A physically-based constitutive model for the shear-dominated response and strain rate effect of carbon fibre reinforced composites. *Composites Part B: Engineering*, *193*, 108032. https://doi.org/10.1016/j.compositesb.2020.108032

Yamashita, S., Sonehara, T., Takahashi, J., Kawabe, K., & Murakami, T. (2017). Effect of thin-ply on damage behaviour of continuous and discontinuous carbon fibre reinforced thermoplastics subjected to simulated lightning strike. *Composites Part A: Applied Science and Manufacturing*, *95*, 132–140. https://doi.org/10.1016/j.compositesa.2017.01.010

Zhao, N., Roy, A., Wang, W., Zhao, L., & Silberschmidt, V. V. (2019). Coupling crystal plasticity and continuum damage mechanics for creep assessment in cr-based power-plant steel. *Mechanics of Materials*, *130*, 29–38. https://doi.org/10.1016/j.mechmat.2019.01.006

APPENDIX A

ANALYTICAL SOLUTION FOR SIMPLE SHEAR TEST

An analytical solution is derived for simple shear test in case of parallel and perpendicular to fibre orientations with respect to loading directions. It is assumed that plane strain conditions hold.

A.1. Loading Parallel to Fibre Direction

2D plane shear case is illustrated in Figure A.1. A horizontal displacement u is applied to the top of the specimen whereas it is restrained at the bottom. Shear strain due to imposed boundary conditions is equal to $\gamma = \tan(\omega) = (u/\mathrm{L})$ where L is the height of the specimen.

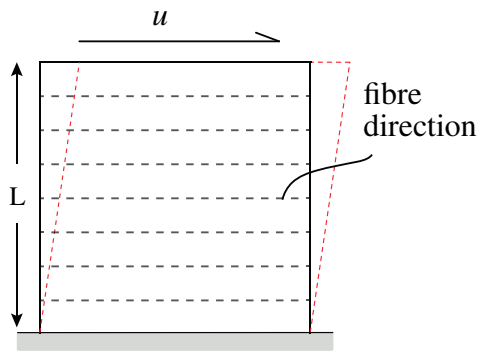

Figure A.1. Illustration of simple shear test for loading parallel to fibre direction. (Deformed shapes are depicted by dashed lines.)

The corresponding mapping function from reference state to deformed configuration can be written as,

$$x_1(t) = \gamma\, X_2(t) + X_1(t)$$
$$x_2(t) = X_2(t) \tag{A.1}$$

The total deformation gradient for simple shear test is defined as

$$\mathbf{F} = \begin{bmatrix} \frac{\partial x_1}{\partial X_1} & \frac{\partial x_1}{\partial X_2} \\ \frac{\partial x_2}{\partial X_1} & \frac{\partial x_2}{\partial X_2} \end{bmatrix} = \begin{bmatrix} 1 & \gamma \\ 0 & 1 \end{bmatrix} \tag{A.2}$$

For pure shear case, plastic deformation gradient is given as follows

$$\mathbf{F}_\mathrm{p} = \begin{bmatrix} 1 & 0 \\ \gamma_p & 1 \end{bmatrix} \tag{A.3}$$

Therefore, elastic deformation gradient can be obtained by using the multiplicative decomposition of deformation gradient,

$$\mathbf{F}_\mathrm{e} = \mathbf{F}\,\mathbf{F}_\mathrm{p}^{-1} = \begin{bmatrix} 1-\gamma\gamma_p & \gamma \\ -\gamma_p & 1 \end{bmatrix} \tag{A.4}$$

Green's strain tensor then follows as,

$$\mathbf{E}_\mathrm{e} = \frac{1}{2}\left(\mathbf{F}_\mathrm{e}^\mathrm{T}\,\mathbf{F}_\mathrm{e} - \mathbf{I}\right) = \frac{1}{2}\begin{bmatrix} \gamma_\mathrm{p}^2 + (\gamma\gamma_\mathrm{p}-1)^2 - 1 & -\gamma_\mathrm{p} - \gamma(\gamma\gamma_\mathrm{p}-1) \\ -\gamma_\mathrm{p} - \gamma(\gamma\gamma_\mathrm{p}-1) & \gamma^2 \end{bmatrix} \tag{A.5}$$

which can be slightly simplified by ignoring terms higher than second-order as

$$\mathbf{E}_\mathrm{e} = \frac{1}{2}\begin{bmatrix} \gamma_\mathrm{p}^2 - 2\gamma\gamma_p & \gamma - \gamma_\mathrm{p} \\ \gamma - \gamma_\mathrm{p} & \gamma^2 \end{bmatrix} \tag{A.6}$$

Second Piola-Kirchhoff stress tensor is calculated by $\mathbf{S} = \mathbb{D} : \mathbf{E}$ and reads as

$$\mathrm{S} = \begin{bmatrix} \frac{E_f}{1-\nu_{12}\nu_{21}}(\mathrm{E}_{11} + \nu_{21}\mathrm{E}_{22}) \\ \frac{E_m}{1-\nu_{12}\nu_{21}}(\nu_{12}\mathrm{E}_{11} + \mathrm{E}_{22}) \\ 2\,G_{12}\mathrm{E}_{12} \end{bmatrix} \tag{A.7}$$

Using $\sigma = \mathrm{J}^{-1}\,\mathbf{F}_\mathrm{e}\,\mathbf{S}\,\mathbf{F}_\mathrm{e}^\mathrm{T}$, Cauchy stress tensor tuns out to be,

$$\sigma_{12} = \begin{cases} G_{12}\,\gamma & \gamma_p = 0 \\ \tau_y & \gamma_p > 0 \end{cases} \tag{A.8}$$

It is to be noted that $\mathrm{J} = \det(\mathbf{F}_\mathrm{e}) = 1$.

A.2. Loading Perpendicular to Fibre Direction

A similar analytical solution can be constructed for the case of a load perpendicular to the direction of the fibres. The case where the imposed displacement is perpendicular to the fibre direction is shown in A.2.

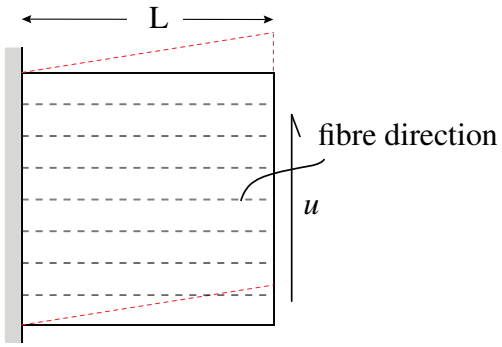

Figure A.2. Illustration of simple shear test for loading parallel to fibre direction. Deformed shapes are depicted by dashed lines.

The corresponding mapping function from reference state to deformed configuration can be written as,

$$\begin{aligned} x_1(t) &= X_1(t) \\ x_2(t) &= \gamma X_1(t) + X_2(t) \end{aligned} \tag{A.9}$$

The total deformation gradient for simple shear test is defined as

$$\mathbf{F} = \begin{bmatrix} \frac{\partial x_1}{\partial X_1} & \frac{\partial x_1}{\partial X_2} \\ \frac{\partial x_2}{\partial X_1} & \frac{\partial x_2}{\partial X_2} \end{bmatrix} = \begin{bmatrix} 1 & 0 \\ \gamma & 1 \end{bmatrix} \tag{A.10}$$

For pure shear case, plastic deformation gradient is given as follows

$$\mathbf{F}_\mathrm{p} = \begin{bmatrix} 1 & \gamma_p \\ 0 & 1 \end{bmatrix} \tag{A.11}$$

It can be decomposed into elastic and plastic parts. Elastic deformation gradient can be obtained by multiplicative decomposition of deformation gradient,

$$\mathbf{F}_\mathrm{e} = \mathbf{F}\,\mathbf{F}_\mathrm{p}^{-1} = \begin{bmatrix} 1 & -\gamma_p \\ \gamma & 1-\gamma\gamma_p \end{bmatrix} \tag{A.12}$$

Green's strain tensor then follows as,

$$\mathbf{E}_\mathrm{e} = 0.5\big(\mathbf{F}_\mathrm{e}^\mathrm{T}\,\mathbf{F}_\mathrm{e} - \mathbf{I}\big) = \frac{1}{2}\begin{bmatrix} \gamma^2 & -\gamma_\mathrm{p} - \gamma(\gamma\gamma_\mathrm{p}-1) \\ -\gamma_\mathrm{p} - \gamma(\gamma\gamma_\mathrm{p}-1) & \gamma_\mathrm{p}^2 + (\gamma\gamma_\mathrm{p}-1)^2 - 1 \end{bmatrix} \tag{A.13}$$

For simplicity, terms higher than second-order are ignored which results in

$$\mathbf{E}_\mathrm{e} = \frac{1}{2}\begin{bmatrix} \gamma^2 & \gamma - \gamma_\mathrm{p} \\ \gamma - \gamma_\mathrm{p} & \gamma_\mathrm{p}^2 - 2\gamma\gamma_p \end{bmatrix} \tag{A.14}$$

Second Piola-Kirchhoff stress tensor is calculated by $\mathbf{S} = \mathbb{D} : \mathbf{E}$ and reads as

$$\mathrm{S} = \begin{bmatrix} \frac{E_f}{1-\nu_{12}\nu_{21}}(\mathrm{E}_{11} + \nu_{21}\mathrm{E}_{22}) \\ \frac{E_m}{1-\nu_{12}\nu_{21}}(\nu_{12}\mathrm{E}_{11} + \mathrm{E}_{22}) \\ 2\,G_{12}\mathrm{E}_{12} \end{bmatrix} \tag{A.15}$$

Using $\sigma = \mathrm{J}^{-1}\,\mathbf{F}_\mathrm{e}\,\mathbf{S}\,\mathbf{F}_\mathrm{e}^\mathrm{T}$, Cauchy stress tensor tuns out to be,

$$\sigma_{12} = \begin{cases} G_{12}\gamma & \gamma_p = 0 \\ \tau_y + 0.5\big(E_f\gamma^3 - E_m\gamma_p^3\big) & \gamma_p > 0 \end{cases} \tag{A.16}$$

It is to be noted that $\mathrm{J} = \det(\mathbf{F}_\mathrm{e}) = 1$. Since the transverse modulus of elasticity is relatively much smaller than the longitudinal modulus of elasticity, the expression can be further simplified by ignoring the part containing E_m .

$$\sigma_{12} = \begin{cases} G_{12}\gamma & \gamma_p = 0 \\ \tau_y + 0.5\,E_f\gamma^3 & \gamma_p > 0 \end{cases} \tag{A.17}$$

APPENDIX B

DERIVATIONS

B.1. Derivation of Local Tangent Stiffness Matrix

In this section, the local tangent stiffness matrix and its components are derived. The residual equation carried by local Newton-Raphson algorithm is given as

$$r^{\eta} = \Delta\gamma^{\eta} - \Delta \mathrm{t}\, \dot{\gamma}_0^{\eta} \left(\frac{|\tau_{n+1}^{\eta}|}{g_{n+1}^{\eta}} \right)^{1/\mathrm{m}} \operatorname{sign}\left(\tau_{n+1}^{\eta}\right) = 0 \tag{B.1}$$

To solve the system of residual equations, the equations are linearized around iteration (k).

$$r^{\eta}|_k + \underbrace{\left.\frac{\partial r^{\eta}}{\partial \Delta\gamma^{\beta}}\right|_k}_{\mathbf{K}} \mathrm{d}\Delta\gamma^{\beta} = 0 \tag{B.2}$$

Linearization of residual equation yields local tangent stiffness which is denoted as $\mathbf{K}$. The tangent stiffness in the local Newton Raphson algorithm is obtained as follows,

$$\begin{aligned} \mathrm{K}^{\eta\beta} = \frac{\partial \mathrm{r}^{\eta}}{\partial \Delta\gamma^{\beta}} + \frac{\partial \mathrm{r}^{\eta}}{\partial \tau_{n+1}^{\alpha}} \frac{\partial \tau_{n+1}^{\alpha}}{\partial \left(\mathbf{F}_{\mathrm{e}}\right)_{n+1}} : \frac{\partial \left(\mathbf{F}_{\mathrm{e}}\right)_{n+1}}{\partial \Delta\gamma^{\beta}} + \\ \frac{\partial \mathrm{r}^{\eta}}{\partial \mathrm{g}_{n+1}^{\alpha}} \frac{\partial \mathrm{g}_{n+1}^{\alpha}}{\partial \mathrm{p}} \frac{\partial \mathrm{p}}{\partial \mathbf{S}_{n+1}} : \frac{\partial \mathbf{S}_{n+1}}{\partial \mathbf{E}_{n+1}} : \frac{\partial \mathbf{E}_{n+1}}{\partial \left(\mathbf{F}_{e}\right)_{n+1}} : \frac{\partial \left(\mathbf{F}_{\mathrm{e}}\right)_{n+1}}{\partial \Delta\gamma^{\beta}} \end{aligned} \tag{B.3}$$

It is worthy to note that $\partial p/\partial \mathbf{E}$ is a local tensor unlike other terms. To overcome this inconsistency, a term consisting partial derivative of $\mathbf{E}^{\mathrm{loc}}$ with respect to $\mathbf{E}^{\mathrm{glob}}$ is inserted next to $\partial \mathbf{S}_{n+1}/\partial \mathbf{E}_{n+1}$. In the following items, derivations of tangent stiffness components are expressed clearly.

- **Derivation of** $\partial \mathrm{r}^{\eta}/\partial \Delta\gamma^{\beta}$

  The expression of residual equation is given in Equation B.1. Partial derivative of

residual equation with respect to slip increments is as follows,

$$\frac{\partial \mathrm{r}^{\eta}}{\partial \Delta\gamma^{\beta}} = \underbrace{\frac{\partial \Delta\gamma^{\eta}}{\partial \Delta\gamma^{\beta}}}_{\delta^{\eta\beta}} - \frac{\partial}{\partial \Delta\gamma^{\beta}} \left(\Delta \mathrm{t}\, \dot{\gamma}_0^{\eta} \left(\frac{|\tau_{n+1}^{\eta}|}{g_{n+1}^{\eta}} \right)^{1/\mathrm{m}} \mathrm{sign}\left(\tau_{n+1}^{\eta}\right) \right) \tag{B.4}$$

Since the second term is independent of $\Delta\gamma^{\beta}$,

$$\frac{\partial \mathrm{r}^{\eta}}{\partial \Delta\gamma^{\beta}} = \delta^{\eta\beta} - 0 = \delta^{\eta\beta} \tag{B.5}$$

- **Derivation of** $\partial \mathbf{F}_{\mathrm{e}} / \partial \Delta\gamma^{\beta}$

Elastic deformation gradient can be calculated based on multiplicative decomposition of deformation gradient into $\mathbf{F}_{\mathrm{e}}$ and $\mathbf{F}_{\mathrm{p}}$.

$$\mathbf{F} = \mathbf{F}_{\mathrm{e}}\, \mathbf{F}_{\mathrm{p}} \tag{B.6}$$

where $\mathbf{F}_{\mathrm{p}}$ can be introduced in terms of slip increments, slip systems and $\left(\mathbf{F}_{\mathrm{p}}\right)_n$. By using exponential map,

$$\left(\mathbf{F}_{\mathrm{p}}\right)_{n+1} = \exp\left(\sum_{\eta=1}^{6} \Delta\gamma^{\eta} \vec{s}_0^{\,\eta} \otimes \vec{n}_0^{\eta} \right) \left(\mathbf{F}_{\mathrm{p}}\right)_n \tag{B.7}$$

$$\mathbf{F}_{\mathrm{e}} = \mathbf{F}\, \mathbf{F}_{\mathrm{p}}^{-1} \tag{B.8}$$

Elastic deformation gradient for t_{n+1} is expressed in terms of slip increments, slip vectors and $\mathbf{F}_{\mathrm{e}}^{\mathrm{trial}}$ which is formed by $\mathbf{F}_{n+1}$ and $(\mathbf{F}_{\mathrm{p}}^{-1})_n$.

$$\left(\mathbf{F}_{\mathrm{e}}\right)_{n+1} = \underbrace{\mathbf{F}_{n+1} \left(\mathbf{F}_{\mathrm{p}}^{-1}\right)_n}_{\mathbf{F}_{\mathrm{e}}^{\mathrm{trial}}} \exp\underbrace{\left(- \sum_{\eta=1}^{6} \Delta\gamma^{\eta} \vec{s}_0^{\,\eta} \otimes \vec{n}_0^{\eta} \right)}_{\mathbf{A}} \tag{B.9}$$

where $\mathbf{A}$ is a second order tensor. Following to steps given below, partial derivative of $\mathbf{F}_{\mathrm{e}}$ with respect to $\Delta\gamma^{\beta}$ can be calculated.

$$\frac{\partial (\mathrm{F}_{\mathrm{e}})_{ij}}{\partial \Delta\gamma^{\beta}} = \left(\mathrm{F}_{\mathrm{e}}^{\mathrm{trial}}\right)_{ik} \frac{\partial \exp(\mathrm{A})_{kj}}{\partial \Delta\gamma^{\beta}} \tag{B.10}$$

$$\frac{\partial \exp(\mathrm{A})_{kj}}{\partial \Delta\gamma^{\beta}} = \frac{\partial \exp(\mathrm{A})_{kj}}{\partial \mathrm{A}_{mn}} : \frac{\partial \mathrm{A}_{mn}}{\partial \Delta\gamma^{\beta}} \tag{B.11}$$

- **Derivation of** $\partial \mathrm{r}^{\eta}/\partial \mathrm{g}^{\alpha}$

  Partial derivative of residual equation with respect to resistance can be calculated by using residual which is given in Equation B.1.

$$\frac{\partial \mathrm{r}^{\eta}}{\partial \mathrm{g}^{\alpha}} = \delta^{\eta\alpha}\,\Delta \mathrm{t}\,\gamma_0^{\eta}\left(\frac{1}{\mathrm{m}}\right)\left(\frac{\left|\tau_{n+1}^{\eta}\right|}{\mathrm{g}_{n+1}^{\eta}}\right)^{(1/\mathrm{m}-1)} \frac{|\tau^{\eta}|}{\left(\mathrm{g}_{n+1}^{\eta}\right)^2}\,\mathrm{sign}\left(\tau_{n+1}^{\eta}\right) \tag{B.12}$$

- **Derivation of** $\partial \mathrm{p}/\partial \mathbf{E}$

  Recall that confinement is a function of second Piola-Kirchhoff stress. It is defined as $\mathrm{p} = -0.5\left(\mathrm{S}_{22} + \mathrm{S}_{33}\right)$ where $\mathbf{S} = \mathbb{D} : \mathbf{E}$. The compliance relation can be written in indicial form as

$$\mathrm{S}_{jk} = \mathrm{D}_{jkmn}\,\mathrm{E}_{mn} \tag{B.13}$$

  Partial derivative of p with respect to **E**,

$$\frac{\partial \mathrm{p}}{\partial \mathrm{E}_{jk}} = -0.5\left(\mathrm{D}_{22jk} + \mathrm{D}_{33jk}\right) \tag{B.14}$$

- **Derivation of** $\partial \mathbf{E}/\partial \mathbf{F}_{\mathrm{e}}$

  Recall that $\mathbf{E} = 0.5\left(\mathbf{C}_{\mathrm{e}} - \mathbf{I}\right)$ where $\mathbf{C}_{\mathrm{e}} = \mathbf{F}_{\mathrm{e}}^{\mathrm{T}}\,\mathbf{F}_{\mathrm{e}}$. Partial derivative of Green strain tensor with respect to elastic deformation gradient produces a 4^{th} order tensor. Calculation steps in indicial notation are presented below.

$$\frac{\partial \mathrm{E}_{jk}}{\partial \left(\mathrm{F}_{\mathrm{e}}\right)_{lm}} = 0.5\left(\frac{\partial \left(\mathrm{F}_{\mathrm{e}}\right)_{vj}^{\mathrm{T}}}{\partial \left(\mathrm{F}_{\mathrm{e}}\right)_{lm}}\left(\mathrm{F}_{\mathrm{e}}\right)_{vk} + \left(\mathrm{F}_{\mathrm{e}}\right)_{vj}^{\mathrm{T}}\frac{\partial \left(\mathrm{F}_{\mathrm{e}}\right)_{vk}}{\partial \left(\mathrm{F}_{\mathrm{e}}\right)_{lm}}\right) \tag{B.15}$$

$$\frac{\partial \mathrm{E}_{jk}}{\partial \left(\mathrm{F}_{\mathrm{e}}\right)_{lm}} = 0.5\left(\delta_{jm}\left(\mathrm{F}_{\mathrm{e}}\right)_{lk} + \delta_{km}\left(\mathrm{F}_{\mathrm{e}}\right)_{lj}^{\mathrm{T}}\right) \tag{B.16}$$

- **Derivation of** $\partial \mathrm{r}^{\eta} / \partial \tau^{\alpha}$

  Recall that residual equation is as follows

$$r^{\eta} = \Delta\gamma^{\eta} - \Delta \mathrm{t}\, \dot{\gamma}_0^{\eta} \left(\frac{|\tau_{n+1}^{\eta}|}{g_{n+1}^{\eta}} \right)^{1/\mathrm{m}} \operatorname{sign}\left(\tau_{n+1}^{\eta}\right) \tag{B.17}$$

  The partial derivative of residual with respect to Schmid stress is as follows,

$$\frac{\partial r^{\eta}}{\partial \tau^{\alpha}} = -\delta^{\eta\alpha} \Delta \mathrm{t}\, \dot{\gamma}_0^{\eta} \frac{1}{\mathrm{m}} \left(\frac{|\tau_{n+1}^{\eta}|}{g_{n+1}^{\eta}} \right)^{1/\mathrm{m}-1} \frac{1}{\mathrm{g}^{\eta}} \operatorname{sign}\left(\tau_{n+1}^{\eta}\right) \operatorname{sign}\left(\tau_{n+1}^{\eta}\right) \tag{B.18}$$

- **Derivation of** $\partial \mathrm{g} / \partial \mathrm{p}$

  Resistance g is a function of p in case confinement pressure is larger than 0. When confinement pressure $\mathrm{p} \geq 0$,

$$\frac{\partial \mathrm{g}^{\alpha}}{\partial \mathrm{p}} = \mu \tag{B.19}$$

  where μ is friction coefficient. Otherwise,

$$\frac{\partial \mathrm{g}^{\alpha}}{\partial \mathrm{p}} = 0 \tag{B.20}$$

- **Derivation of** $\partial \tau^{\alpha} / \partial \mathbf{F}_{\mathrm{e}}$

  Recall that Schmid stress is a function of Kirchhoff stress tensor and slip systems.

$$\tau^{\alpha} = \boldsymbol{\tau} : \left(\vec{s}^{\,\alpha} \otimes \vec{n}^{\alpha} \right) \tag{B.21}$$

  where *s* and *n* are slip vectors in current frame. Equation B.21 can be written in terms of indicial notation as follows,

$$\tau^{\alpha} = \tau_{mn}\, s_m^{\alpha}\, n_n^{\alpha} \tag{B.22}$$

  The partial derivative of Schmid stress with respect to $\mathbf{F}_{\mathrm{e}}$,

$$\frac{\partial \tau^{\alpha}}{\partial \left(\mathrm{F_e}\right)_{jk}} = \underbrace{\frac{\partial \tau_{mn}}{\partial \left(\mathrm{F_e}\right)_{jk}} s_m^{\alpha} n_n^{\alpha}}_{\text{Term I}} + \underbrace{\tau_{mn} \frac{\partial s_m^{\alpha}}{\partial \left(\mathrm{F_e}\right)_{jk}} n_n^{\alpha}}_{\text{Term II}} + \underbrace{\tau_{mn}\, s_m^{\alpha} \frac{\partial n_n^{\alpha}}{\partial \left(\mathrm{F_e}\right)_{jk}}}_{\text{Term III}} \tag{B.23}$$

– Obtaining the Term I

$$\left(\text{Term I}\right)^{\alpha}_{jk} = \mathrm{A}_{mnjk}\, s^{\alpha}_{m} n^{\alpha}_{n} \tag{B.24}$$

where $\mathbb{A}$ is the partial derivative of Kirchhoff stress tensor with respect to elastic deformation gradient which is given in Equation B.37.

– Obtaining the Term II

Slip vectors in current configuration are function of $\mathbf{F}_{\mathrm{e}}$ and s^{α}_{0} as they are formulated in Equation B.25.

$$s^{\alpha} = \mathbf{F}_{\mathrm{e}}\, s^{\alpha}_{0} \tag{B.25}$$

Partial derivatives of slip vectors in current configuration with respect to $\mathbf{F}_{\mathrm{e}}$ are derived below.

$$\frac{\partial s^{\alpha}_{m}}{\partial \left(\mathrm{F_e}\right)_{jk}} = \underbrace{\frac{\partial \left(\mathrm{F_e}\right)_{mv}}{\partial \left(\mathrm{F_e}\right)_{jk}}}_{\delta_{mj}\,\delta_{vk}} \left(s_0\right)^{\alpha}_{v} \tag{B.26}$$

Equation B.26 is implemented to Term II,

$$\left(\text{Term II}\right)^{\alpha}_{jk} = \tau_{jn} \left(s_0\right)^{\alpha}_{k} n^{\alpha}_{n} \tag{B.27}$$

– Obtaining the Term III

$$\left(\text{Term III}\right)^{\alpha}_{jk} = \tau_{mn}\, s^{\alpha}_{m} \frac{\partial n^{\alpha}_{n}}{\partial \left(\mathrm{F_e}\right)_{jk}} \tag{B.28}$$

Normal slip vectors in current configuration are function of $\mathbf{F}_{\mathrm{e}}$ and n^{α}_{0} as they are formulated as

$$n^{\eta} = \mathbf{F}^{-\mathrm{T}}_{\mathrm{e}}\, n^{\eta}_{0} \tag{B.29}$$

Partial derivative of n^{α} with respect to $\mathbf{F}_{\mathrm{e}}$ is as follows,

$$\frac{\partial n_n^{\alpha}}{\partial \left(\mathrm{F_e}\right)_{jk}} = \left(n_0^{\alpha}\right)_v \underbrace{\frac{\partial \left(\mathrm{F_e}\right)_{vn}^{-1}}{\partial \left(\mathrm{F_e}\right)_{jk}}}_{\mathbb{A}} \tag{B.30}$$

where $\mathbb{A}$ is a fourth-order tensor and yields as

$$\frac{\partial \left(\mathrm{F_e}\right)_{vn}^{-1}}{\partial \left(\mathrm{F_e}\right)_{jk}} = -\left(\mathrm{F_e}\right)_{vj}^{-1} \left(\mathrm{F_e}\right)_{kn}^{-1} \tag{B.31}$$

Term III is presented below.

$$\left(\text{Term III}\right)_{jk}^{\alpha} = -\tau_{mn}\, s_m^{\alpha} \left(n_0^{\alpha}\right)_v \left(\mathrm{F_e}\right)_{vj}^{-1} \left(\mathrm{F_e}\right)_{kn}^{-1} \tag{B.32}$$

- **Derivation of** $\partial \mathbf{A}^{\mathrm{loc}} / \partial \mathbf{A}^{\mathrm{glob}}$

  This term is the partial derivative of a local second order tensor with respect to its global form. It is stated that $\mathbf{A}$ is a second order tensor, and the term produces a fourth order tensor. Transformation of a second order tensor in global to local configuration is given in B.42.

$$\mathbf{A}^{\mathrm{loc}} = \mathbf{Q}\, \mathbf{A}^{\mathrm{glob}}\, \mathbf{Q}^{\mathrm{T}} \tag{B.33}$$

$$\frac{\partial \mathbf{A}^{\mathrm{loc}}}{\partial \mathbf{A}^{\mathrm{glob}}} = \frac{\partial \left(\mathbf{Q}\, \mathbf{A}^{\mathrm{glob}}\, \mathbf{Q}^{\mathrm{T}}\right)}{\partial \mathbf{A}^{\mathrm{glob}}} \tag{B.34}$$

  where $\mathbf{Q}$ is a second order transformation tensor. Expression can be written in indicial notation as follows

$$\frac{\partial \mathrm{A}_{jk}^{\mathrm{loc}}}{\partial \mathrm{A}_{mn}^{\mathrm{glob}}} = \mathrm{Q}_{jv}\mathrm{Q}_{ky} \frac{\partial \mathrm{A}_{vy}}{\partial \mathrm{A}_{mn}} = \mathrm{Q}_{jm}\mathrm{Q}_{kn} \tag{B.35}$$

- **Derivation of** $\partial \boldsymbol{\tau} / \partial \mathbf{F}_{\mathrm{e}}$

  The Kirchhoff stress is a function of $\mathbf{F}_{\mathrm{e}}$ and $\mathbf{S}$. It is defined as

$$\boldsymbol{\tau} = \mathbf{F}_{\mathrm{e}}\, \mathbf{S}\, \mathbf{F}_{\mathrm{e}}^{\mathrm{T}} \tag{B.36}$$

Partial derivative of $\boldsymbol{\tau}$ with respect to $\mathbf{F}_\mathrm{e}$,

$$\frac{\partial \boldsymbol{\tau}}{\partial \mathbf{F}_\mathrm{e}} = \underbrace{\frac{\partial \mathbf{F}_\mathrm{e}}{\partial \mathbf{F}_\mathrm{e}} \mathbf{S}\, \mathbf{F}_\mathrm{e}^\mathrm{T}}_{\text{Term-I}} + \underbrace{\mathbf{F}_\mathrm{e} \frac{\partial \mathbf{S}}{\partial \mathbf{F}_\mathrm{e}} \mathbf{F}_\mathrm{e}^\mathrm{T}}_{\text{Term-II}} + \underbrace{\mathbf{F}_\mathrm{e}\, \mathbf{S}\, \frac{\partial \mathbf{F}_\mathrm{e}^\mathrm{T}}{\partial \mathbf{F}_\mathrm{e}}}_{\text{Term-III}} \tag{B.37}$$

– Obtaining Term I,

$$\left(\text{Term I}\right)_{jkmn} = \underbrace{\frac{\partial \left(\mathrm{F_e}\right)_{jp}}{\partial \left(\mathrm{F_e}\right)_{mn}}}_{\delta_{jm}\,\delta_{pn}} \mathrm{S}_{pt} \left(\mathrm{F_e}\right)_{kt} = \delta_{jm}\, \mathrm{S}_{nt} \left(\mathrm{F_e}\right)_{kt} \tag{B.38}$$

– Obtaining Term II,

$$\left(\text{Term II}\right)_{jkmn} = \left(\mathrm{F_e}\right)_{jp} \frac{\partial \mathrm{S}_{pt}}{\partial \left(\mathrm{F_e}\right)_{mn}} \left(\mathrm{F_e}\right)_{kt} \tag{B.39}$$

where

$$\frac{\partial \mathrm{S}_{pt}}{\partial \left(\mathrm{F_e}\right)_{mn}} = \mathbb{D}_{ptrs} \frac{\partial \mathrm{E}_{rs}}{\partial \left(\mathrm{F_e}\right)_{mn}} \tag{B.40}$$

Partial derivative of Green's strain tensor with respect to elastic deformation gradient is given in Equation B.16.

– Obtaining Term III,

$$\left(\text{Term III}\right)_{jkmn} = \left(\mathrm{F_e}\right)_{jp} \mathrm{S}_{pt} \frac{\partial \left(\mathrm{F_e}\right)_{kt}}{\partial \left(\mathrm{F_e}\right)_{mn}} = \left(\mathrm{F_e}\right)_{jp} \mathrm{S}_{pn}\, \delta_{km} \tag{B.41}$$

This is how the 4^{th} order $\partial\boldsymbol{\tau}/\partial\mathbf{F}_e$ tensor is obtained. It should be noted that Green's strain tensor is a global quantity since deformation gradient obtained from Abaqus is in global form. However, there is a local material tensor in constitutive relation. To overcome this situation, applied procedure is given below.

Algorithm 4 Local to global transformation

Transform $\mathbf{E}^{\text{glob}}$ to $\mathbf{E}^{\text{loc}}$ (See Equation B.42)

Obtain second Piola-Kirchoff stress in local form, $\mathbf{S}^{\text{loc}} = \mathbb{D} : \mathbf{E}^{\text{loc}}$

Transform $\mathbf{S}^{\text{loc}}$ to $\mathbf{S}^{\text{glob}}$ (See Equation B.44)

- Transformation of $\mathbf{A}^{\text{glob}}$ to $\mathbf{A}^{\text{loc}}$

  A second order tensor $\mathbf{A}$ can be transformed into local frame from the global frame by using

$$\mathbf{A}^{\text{loc}} = \mathbf{Q}\,\mathbf{A}^{\text{glob}}\,\mathbf{Q}^{\text{T}} \tag{B.42}$$

  where $\mathbf{Q}$ is the transformation matrix and defined below.

$$\mathbf{Q} = \begin{bmatrix} \cos\phi & \sin\phi & 0 \\ -\sin\phi & \cos\phi & 0 \\ 0 & 0 & 1 \end{bmatrix} \tag{B.43}$$

  where ϕ is the angle between global and local frames.

- Transformation of $\mathbf{A}^{\text{loc}}$ to $\mathbf{A}^{\text{glob}}$

  A second order tensor $\mathbf{A}$ can be transformed into global frame from the local frame

$$\mathbf{A}^{\text{glob}} = \mathbf{Q}^{\text{T}}\,\mathbf{A}^{\text{loc}}\,\mathbf{Q} \tag{B.44}$$

  where $\mathbf{Q}$ is defined in Equation B.43.

B.2. Derivation of Material Tangent Stiffness

In this section material tangent stiffness matrix is derived. Recall that internal virtual work is as follows

$$\delta W_{int} = \int_V \boldsymbol{\tau}_{n+1} : \left(\nabla_0\,\delta\mathbf{u}\left(\mathbf{F}^{-1}\right)_{n+1}\right) \mathrm{d}V \tag{B.45}$$

Directional derivative of internal virtual work in the direction of $[\Delta\mathbf{u}]$,

$$\mathrm{D}\big(\delta W_{int}\big)[\Delta\mathbf{u}] = \mathrm{D}\left(\boldsymbol{\tau}_{n+1}\right)[\Delta\mathbf{u}] : \nabla_0\delta\mathbf{u}\,\mathbf{F}^{-1} + \boldsymbol{\tau}_{n+1} : \mathrm{D}\big(\nabla_0\delta\mathbf{u}\,\mathbf{F}^{-1}\big)[\Delta\mathbf{u}] \tag{B.46}$$

where the left term produces material tangent stiffness matrix.

$$\mathrm{D}\left(\boldsymbol{\tau}_{n+1}\right)[\Delta\mathbf{u}] \;=\; \underbrace{\frac{\partial\boldsymbol{\tau}_{n+1}}{\partial\mathbf{F}_{n+1}}}_{\left(\mathbb{D}_{\mathrm{mat}}\right)_{n+1}} \;:\; \mathrm{D}\left(\mathbf{F}_{n+1}\right)[\Delta\mathbf{u}] \tag{B.47}$$

Kirchhoff stress is a function of $\mathbf{F_e}$ and $\Delta\gamma^{\beta}$. Therefore, $(\mathbb{D}_{\mathrm{mat}})_{n+1}$ can be calculated by the chain rule as,

$$\frac{\partial\boldsymbol{\tau}_{n+1}}{\partial\mathbf{F}_{n+1}} = \underbrace{\frac{\partial\boldsymbol{\tau}_{n+1}}{\partial\left(\mathbf{F}_{\mathrm{e}}\right)_{n+1}}}_{\mathbb{A}1} : \frac{\partial\left(\mathbf{F}_{\mathrm{e}}\right)_{n+1}}{\partial\mathbf{F}_{n+1}}\bigg|_{\Delta\gamma^{\beta}} + \frac{\partial\boldsymbol{\tau}_{n+1}}{\partial\left(\mathbf{F}_{\mathrm{e}}\right)_{n+1}} : \underbrace{\frac{\partial\left(\mathbf{F}_{\mathrm{e}}\right)_{n+1}}{\partial\Delta\gamma^{\beta}}\bigg|_{\mathbf{F}_{n+1}}}_{\mathbf{A2}} : \frac{\partial\Delta\gamma^{\beta}}{\partial\mathbf{F}_{n+1}} \tag{B.48}$$

The terms $\mathbb{A}1$ and $\mathbf{A2}$ are derived in Equation B.37 and Equation B.10, respectively. In the following items, derivations of remaining components are expressed clearly.

- **Derivation of** $\partial\mathbf{F}_{\mathrm{e}}/\partial\mathbf{F}$

  The expression of $\mathbf{F}_{\mathrm{e}}$ is defined below,

$$\left(\mathbf{F}_{\mathrm{e}}\right)_{n+1} = \mathbf{F}_{n+1}\left(\mathbf{F}_{\mathrm{p}}^{-1}\right)_{n}\exp\left(-\sum_{\eta=1}^{6}\Delta\gamma^{\eta}\vec{s}_{0}^{\,\eta}\otimes\vec{n}_{0}^{\eta}\right) \tag{B.49}$$

  Partial derivative of $\mathbf{F}_{\mathrm{e}}$ with respect to $\mathbf{F}$ as follows,

$$\frac{\partial\mathbf{F}_{\mathrm{e}}}{\partial\mathbf{F}} = \frac{\partial\mathbf{F}}{\partial\mathbf{F}}\left(\mathbf{F}_{\mathrm{p}}^{-1}\right)\exp\left(-\sum_{\eta=1}^{6}\Delta\gamma^{\eta}\vec{s}_{0}^{\,\eta}\otimes\vec{n}_{0}^{\eta}\right) \tag{B.50}$$

- **Derivation of** $\partial\Delta\gamma^{\beta}/\partial\mathbf{F}$

  When the material disturbed by $\mathrm{d}\mathbf{F}_{n+1}$, the residual equations pertaining to slip systems should be satisfied. Since residual is functions of $\mathbf{F}_{\mathrm{e}}$ and $\Delta\gamma^{\eta}$,

$$\left[\frac{\partial r^{\eta}}{\partial\Delta\gamma^{\beta}}\bigg|_{\mathbf{F}_{n+1}}\frac{\partial\Delta\gamma^{\beta}}{\partial\mathbf{F}_{n+1}} + \frac{\partial r^{\eta}}{\partial\mathbf{F}_{n+1}}\bigg|_{\Delta\gamma^{\beta}}\right] : \mathrm{d}\mathbf{F}_{n+1} = 0 \tag{B.51}$$

  Since the disturbance ($\mathrm{d}\mathbf{F}_{n+1}$) is always non-zero, the term in square brackets must be

equal to $\mathbf{0}$.

$$\Bigg[\underbrace{\left.\frac{\partial r^{\eta}}{\partial \Delta\gamma^{\beta}}\right|_{\mathbf{F}_{n+1}}}_{\mathrm{K}^{\eta\beta}} \frac{\partial \Delta\gamma^{\eta}}{\partial \mathbf{F}_{n+1}} + \underbrace{\left.\frac{\partial r^{\eta}}{\partial \mathbf{F}_{n+1}}\right|_{\Delta\gamma^{\beta}}}_{\mathbf{G}^{\eta}} \Bigg] = \mathbf{0} \tag{B.52}$$

$$\mathrm{K}^{\eta\beta} \frac{\partial \Delta\gamma^{\beta}}{\partial \mathbf{F}_{n+1}} + \mathbf{G}^{\eta} = \mathbf{0} \tag{B.53}$$

Terms $\mathrm{K}^{\eta\beta}$ and $\mathbf{G}^{\eta}$ are derived in Equation B.3 and Equation B.55, respectively.

$$\frac{\partial \Delta\gamma^{\xi}}{\partial \mathbf{F}_{n+1}} = -\left(\mathrm{K}^{-1}\right)^{\xi\eta} \mathbf{G}^{\eta} \tag{B.54}$$

- **Derivation of $\mathbf{G}^{\eta}$**

  In an open form, $\mathbf{G}^{\eta}$ can be written as

$$\mathbf{G}^{\eta} = \frac{\partial r^{\eta}}{\partial g^{\alpha}_{n+1}} \frac{\partial g^{\alpha}_{n+1}}{\partial \mathrm{p}} \frac{\partial \mathrm{p}}{\partial \mathbf{S}_{n+1}} : \frac{\partial \mathbf{S}_{n+1}}{\partial \mathbf{E}_{n+1}} : \frac{\partial \mathbf{E}_{n+1}}{\partial (\mathbf{F}_{\mathrm{e}})_{n+1}} : \underbrace{\left.\frac{\partial (\mathbf{F}_{\mathrm{e}})_{n+1}}{\partial \mathbf{F}_{n+1}}\right|_{\Delta\gamma^{\beta}}}_{\mathbb{A}} \tag{B.55}$$

  All terms except $\mathbb{A}$ are derived in items under Appendix-B.1. The expression of $\mathbf{F}_{\mathrm{e}}$ is defined below,

$$\left(\mathbf{F}_{\mathrm{e}}\right)_{n+1} = \underbrace{\mathbf{F}_{n+1} \left(\mathbf{F}_{\mathrm{p}}^{-1}\right)_{n}}_{\mathbf{F}_{\mathrm{e}}^{\mathrm{trial}}} \underbrace{\exp\left(- \sum_{\eta=1}^{6} \Delta\gamma^{\eta} \vec{s}_{0}^{\,\eta} \otimes \vec{n}_{0}^{\eta} \right)}_{\mathbf{B}} \tag{B.56}$$

  The partial derivative of $\mathbf{F}_{\mathrm{e}}$ with respect to deformation gradient matrix is as follows

$$\frac{\partial \left(\mathbf{F}_{\mathrm{e}}\right)_{n+1}}{\partial \mathbf{F}_{n+1}} = \left. \frac{\partial \left(\mathrm{F}_{ij} \left(\mathrm{F}_{\mathrm{p}}\right)^{-1}_{jq} \mathrm{B}_{qp} \right)}{\partial \mathrm{F}_{kl}} \right|_{\Delta\gamma^{\beta}} \tag{B.57}$$

$$\frac{\partial \left(\mathbf{F}_{\mathrm{e}}\right)_{n+1}}{\partial \mathbf{F}_{n+1}} = \delta_{ik} \left(\mathrm{F}_{\mathrm{p}}\right)^{-1}_{lq} \mathrm{B}_{qp} \tag{B.58}$$

B.3. Derivation of Geometric Tangent Stiffness

As stated previously, the term $\left(\boldsymbol{\tau} : \mathrm{D}\left(\nabla_0 \delta\mathbf{u}\,\mathbf{F}^{-1}\right)[\Delta\mathbf{u}]\right)$ in Equation B.46 leads to geometric tangent stiffness. Geometric tangent stiffness can be calculated by following the equations given below.

$$\mathrm{D}\left(\nabla_0 \delta\mathbf{u}\,\mathbf{F}^{-1}\right)[\Delta\mathbf{u}] = -\delta u_{i,j}\,\mathrm{F}^{-1}_{jk}\,\Delta u_{k,l}\,\mathrm{F}^{-1}_{lm} \tag{B.59}$$

$$\boldsymbol{\tau} : \mathrm{D}\left(\nabla_0 \delta\mathbf{u}\,\mathbf{F}^{-1}\right)[\Delta\mathbf{u}] = -\tau_{im}\,\delta u_{i,j}\,\mathrm{F}^{-1}_{jk}\,\Delta u_{k,l}\,\mathrm{F}^{-1}_{lm}$$

$$\boldsymbol{\tau} : \mathrm{D}\left(\nabla_0 \delta\mathbf{u}\,\mathbf{F}^{-1}\right)[\Delta\mathbf{u}] = -\delta u_{i,j}\,\underbrace{\mathrm{F}^{-1}_{jk}\,\tau_{im}\,\mathrm{F}^{-\mathrm{T}}_{ml}}_{\mathrm{C}^{G}_{jkil}}\,\Delta u_{k,l} \tag{B.60}$$

As described in following equation, $\mathbb{C}_{\mathrm{geo}}$ can be obtained by rearranging the cells of C^{G}_{jkil}.

$$\left(\mathbf{C}_{\mathrm{geo}}\right)_{ijkl} \leftarrow \mathrm{C}^{G}_{jkil} \tag{B.61}$$